Efficient and sustained optogenetic control of nervous and cardiac systems

Maria Zerche[1,2,3,4*], Victoria Hunniford[1,4,5*], Alexey Alekseev[1,3,4*], Fadhel El May[1*], Anna Vavakou[1,4,*], Dominique Siegenthaler[4,6,7*], Marc A. Hüser[2,8**], Svenja M. Kiehn[8**], Aida Garrido-Charles[1,3**], Theocharis Alvanos[1,5,**], Isabel Witzke[1,3], Stuart Trenholm[9], Emilie Macé[4,6,7], Kathrin Kusch[1,10], Tobias Bruegmann[4,8,11], Bettina J. Wolf[1,4,5,12#], Thomas Mager[1,3,4#], and Tobias Moser[1,4,5,12#]

[1]Institute for Auditory Neuroscience and InnerEarLab, University Medical Center Göttingen, Germany

[2]Department of Otolaryngology, University Medical Center Göttingen, Germany

[3]Advanced Optogenes Group, Institute for Auditory Neuroscience, University Medical Center Göttingen, Germany

[4]Cluster of Excellence "Multiscale Bioimaging: from Molecular Machines to Networks of Excitable Cells" (MBExC), University of Göttingen, Germany

[5]Auditory Neuroscience and Synaptic Nanophysiology Group, Max-Planck-Institute for Multidisciplinary Sciences, Göttingen, Germany

[6]Brain-Wide Circuits for Behavior Research Group, Max Planck Institute for Biological Intelligence, Planegg, Germany

[7]Dynamics of Excitable Cell Networks Group, Department of Ophthalmology, University Medical Center Göttingen, Göttingen, Germany

[8]Institute for Cardiovascular Physiology, University Medical Center Göttingen, Göttingen, Germany

[9]Montreal Neurological Institute, McGill University, Montreal, Canada

[10]Functional Auditory Genomics Group, Auditory Neuroscience and Optogenetics laboratory, German Primate Center, Göttingen, Germany

[11]German Center for Cardiovascular Research (DZHK), Partner site Göttingen, Göttingen, Germany

[12]Auditory Neuroscience and Optogenetics laboratory, German Primate Center, Göttingen, Germany

[*]shared first, [**]shared second, [#]shared corresponding

Abstract

Optogenetic control of cells is a key life sciences method and promises novel therapies. Here we report on ChReef, an improved variant of the channelrhodopsin ChRmine, enabling efficient (nano-Joule) and sustained optogenetic stimulation of excitable cells. ChReef offers minimal photocurrent desensitization, a unitary conductance of 80 fS and closing kinetics of 30 ms, which together enable reliable optogenetic control of cardiac and nervous systems at low light levels with good temporal fidelity. We demonstrate efficient and reliable red-light pacing and depolarization block of ChReef-expressing cardiomyocyte clusters. ChReef-expression in the optic nerve restores visual function in blind mice with light sources as weak as an iPad screen. ChReef enables stimulation of the auditory nerve at up to 50-100 Hz with good temporal precision and low pulse energy threshold (170 nJ) close that of electrical stimulation (50 nJ). Thus, ChReef outperforms ChRmine and bears great potential for life sciences and clinical application.

Keywords: channelrhodopsin, automated patch-clamp, neural circuit, hearing, vision, cardiac defibrillation

Running title:

Efficient optogenetic control of heart and brain

Introduction

With an ever-growing toolkit of light-sensitive proteins (opsins) and optical devices, optogenetics has become a major driver of progress in the life sciences[1]. It is routinely used to manipulate the activity of specific cell types *in vivo* in genetically tractable species such as mice, fish, or flies. In medicine, concurring progress in optogenetic modification of retinal neurons and visual coding by light amplifying goggles has enabled a first successful clinical application of optogenetics for vision restoration[2]. Yet, several challenges remain to be tackled for realizing the full potential of optogenetics. For example, the low single-channel conductance of non-selective cation conducting channelrhodopsins (ChRs: e.g. 40 fS for ChR2[3]) limits their utility. The required high levels of expression and high light doses bear the risk of proteostatic stress and phototoxicity in the target tissue[4]. In the visual system, low single-channel conductance impedes versatile optogenetic stimulation by natural light or computer screens and necessitates the use of light amplifying goggles for optogenetic vision restoration. The energy demand of state-of-the-art optogenetic control also challenges the power budget of medical devices such as future optical cochlear implants for improved hearing restoration[4,5]. Kalium- and Anion-selective cryptophyte channelrhodopsins (KCRs and ACRs) with larger single channel conductance have recently been reported serving efficient inhibition of excitable cells[6,7]. Aiming for a depolarizing ChR for efficient excitation, we targeted the cryptophyte ChR ChRmine that mediates large depolarizing photocurrents and has red-shifted light absorption (λ_{max} = 520 nm)[8–10]. This way ChRmine, for example, has enabled control of cardiac activity of mice by light applied from outside[11] as well as implant-free deep brain optogenetics[12]. Yet, strong desensitization is an unsolved key problem of ChRmine, impeding applications that require sustained or high rate optogenetic stimulation.

Here, we deciphered mechanistic underpinnings of the shortcomings of ChRmine and generated mutants that overcome them resulting in advanced utility when applied to the heart, the eye, and the ear.

Results

ChRmine is a high unitary conductance ChR that exhibits strong light-dependent inactivation

Using patch-clamp recordings from neuroblastoma-glioma cells (NG cells) expressing ChRmine fused to TS-EYFP-ES for improved plasma membrane targeting[8,13,14], we found that the stationary photocurrent of ChRmine is only about 20% of the peak current (Stationary-Peak-Ratio: 0.22 ± 0.12 (n = 57), Fig. 1a, Figs. S2 and S5, Table S1). In fact, the ChRmine stationary photocurrent density at saturating light intensity (Fig. 1c, $J_{-60mV} = 21.6 \pm 15.8$ pA/pF, n = 44) did not exceed that of other state of the art depolarizing ChRs (Fig. 1d, Table S2). Interestingly, the stationary photocurrent showed an initial increase with light intensity followed by a decrease to a submaximal value despite increasing light intensity (Fig. 1b), suggesting a substrate (photon) inhibition of the partial type[15] that had, to our knowledge, not yet been described previously.

As the unitary conductance of ChRs is too small to be directly determined by single channel recordings, we investigated the variance in photocurrent ensembles using stationary and non-stationary noise analysis[16]. As ChR conductance approaches the detection limit in stationary noise analysis[3,6,7,17], we upscaled data collection by automated patch-clamp (Syncropatch 384, Nanion) operated in synchrony with LED-based illumination. This way, we could simultaneously record ensembles of photocurrents from dozens of HEK293 cells (holding potential: −100 mV) elicited by blue light for the efficient ChR2 mutant CatCh[17] or green light for ChRmine (Fig. S3).

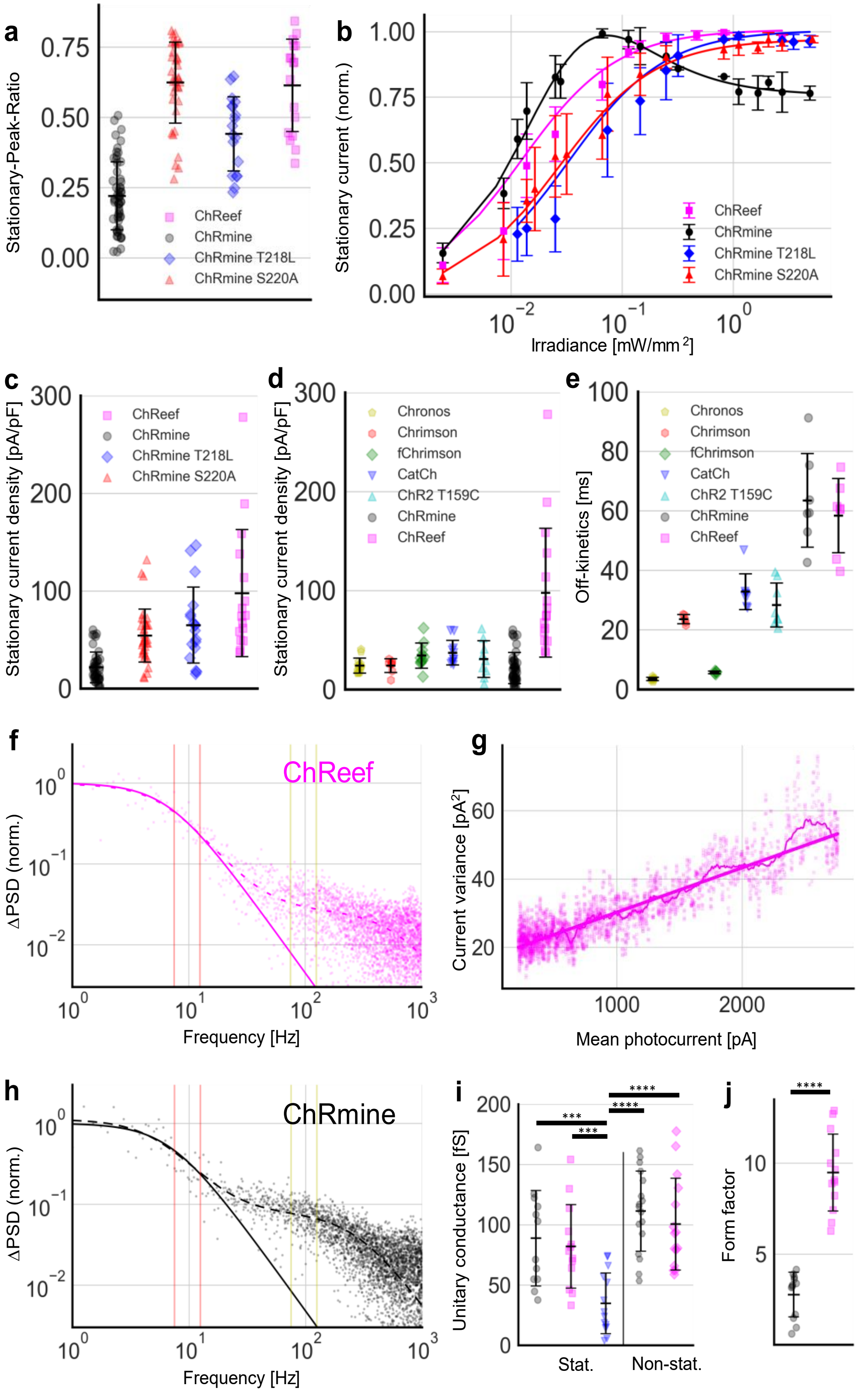
a
Stationary-Peak-Ratio
0.00
0.25
0.50
0.75
ChReef
ChRmine
ChRmine T218L
ChRmine S220A
b
Stationary current (norm.)
0.00
0.25
0.50
0.75
1.00
10^{-2}
10^{-1}
10^{0}
Irradiance [mW/mm^2]
ChReef
ChRmine
ChRmine T218L
ChRmine S220A
c
Stationary current density [pA/pF]
0
100
200
300
ChReef
ChRmine
ChRmine T218L
ChRmine S220A
d
Stationary current density [pA/pF]
0
100
200
300
Chronos
Chrimson
fChrimson
CatCh
ChR2 T159C
ChRmine
ChReef
e
Off-kinetics [ms]
0
20
40
60
80
100
Chronos
Chrimson
fChrimson
CatCh
ChR2 T159C
ChRmine
ChReef
f
ChReef
ΔPSD (norm.)
10^{0}
10^{-1}
10^{-2}
10^{0}
10^{1}
10^{2}
10^{3}
Frequency [Hz]
g
Current variance [pA^2]
20
40
60
1000
2000
Mean photocurrent [pA]
h
ChRmine
ΔPSD (norm.)
10^{0}
10^{-1}
10^{-2}
10^{0}
10^{1}
10^{2}
10^{3}
Frequency [Hz]
i
Unitary conductance [fS]
0
50
100
150
200
***
***
****
****
Stat.
Non-stat.
j
Form factor
5
10
****

Figure 1. Electrophysiological characterization of ChRmine variants. a-e, Photocurrents of NG cells expressing channelrhodopsin variants were elicited at saturating light intensity (λ = 532 nm) and recorded by whole-cell patch-clamp at a membrane potential of -60 mV. **a**, Stationary-Peak-Ratios of the photocurrents of ChRmine-TS-EYFP-ES (“ChRmine”, black circle, n=57), ChRmine-TS-EYFP-ES S220A (“ChRmine S220A”, red triangle, n=38), ChRmine-TS-EYFP-ES T218L (“ChRmine T218L”, blue rhombus, n=18) and ChRmine-TS-EYFP-ES T218L/S220A (“ChReef”, magenta square, n=21). **b**, Light intensity dependence of the normalized stationary photocurrents of ChRmine (n=7), ChRmine S220A (n=4), ChRmine T218L (n=4) and ChReef (n=4) (λ = 532 nm). The solid lines colored in red, blue, and magenta show fits to the data using a hyperbolic function. The black solid line shows a fit to the data using an equation describing a substrate inhibition of the partial type (see online methods). **c**, Current densities of ChRmine variants: stationary photocurrent densities of ChRmine (n=44), ChRmine S220A (n=35), ChRmine T218L (n=18) and ChReef (n=16) at saturating light intensity. (λ = 532 nm) **d**, Stationary photocurrent densities of Chronos-EYFP (yellow pentagon, λ = 473 nm, n=14), Chrimson-EYFP (red hexagon, λ = 594 nm, n=8, f-Chrimson-EYFP (green rhombus, λ = 594 nm, n=11, [18]), CatCh-EYFP (blue triangle, λ = 473 nm, n=11) and ChR2-EYFP T159C (cyan triangle, λ = 473 nm, n=9) at saturating light intensities, ChRmine and ChReef replotted for comparison. **e**, Channel closing kinetics of ChR variants. τ_{off} values of Chronos-EYFP (pentagon, λ = 473 nm, n=8), Chrimson-EYFP (λ = 594 nm, n=5 [from ref. [18]]), f-Chrimson-EYFP (λ = 594 nm, n=5, [from ref. [18]]), CatCh-EYFP (λ = 473 nm, n=9) and ChR2-EYFP T159C (λ = 473 nm, n=8), ChRmine (λ = 532 nm, n=7) and ChReef (λ = 532 nm, n=7). **f-j**, Noise analysis of ChRmine and ChReef photocurrents. **f, h**, Exemplary plots showing the difference of the power spectral densities (PSD) of whole-cell currents recorded from HEK293T cells expressing ChReef **(f)** or ChRmine **(h)** under light and dark conditions at a membrane potential of -100 mV. The PSD difference was normalized to the fitted value at 0 Hz. Solid lines: fit to the PSD difference by a single Lorentzian function, dashed line: fit by a double Lorentzian function. **g**, Non-stationary noise analysis of whole-cell photocurrents recorded at a membrane potential of -100 mV: relation between the variance of an exemplary ChReef photocurrent and its average value. Thin line: moving average of the variance, bold line: linear fit to the data. **I**, Statistical comparison of single channel conductance values of ChRmine, ChReef and CatCh obtained by stationary (grey circles for ChRmine, magenta squares for ChReef and blue triangles for CatCh) and non-stationary (grey hexagons for ChRmine and magenta diamonds for ChReef) noise analyses. **j**, Statistical comparison of PSD form factor values for ChRmine (grey circles) and ChReef (magenta squares). The form factor is defined as the ratio of mean ΔPSD values at 7.5 to 12.5 Hz (region between the red lines depicted in panels a and c) and 75 to 125 Hz (region between the yellow lines depicted in panels f and g). (p-value < 0.05 (*), 0.005 (**), 0.001 (***), 0.0001(****), the comparisons were done using Tukey´s HSD (honestly significant difference test). **a-j**, The symbols in **(b)** and horizontal bars in **(a, c-e, i, j)** indicate average values, the error bars show SD **(a-e, i, j).**

Strict quality measures, regarding background noise ($I_{RMS,\ dark} < 5.5$ pA) and stationary photocurrent size (> 200 pA), limited the number of suitable recordings to 14/149 for CatCh and 12/71 for ChRmine. Still, a sample size sufficing statistical comparison could be obtained within days, due to the highly parallelized approach. Fitting the power spectra with Lorentzian functions revealed a significantly larger single channel conductance of ChRmine compared to CatCh (Fig. 1h, i, ChRmine: 88.8 ± 39.6 fS, n=12 vs. CatCh: 34.8 ± 25.1 fS, n=14, $p < 0.001$). We confirmed this finding by non-stationary noise analysis (Fig. 1g, 111.3 ± 33.2 fS (n=17); holding potential: −100 mV) using short (5 ms) light pulses at a rate of 0.2 Hz to avoid desensitization. The stationary noise analysis provided further insight into ChRmine function: in addition to the power spectral density in the low frequency range (2.5 to 25 Hz) it also exhibited a pronounced shoulder at higher frequencies (75 to 125 Hz – yellow lines, Fig. 1h, j). This likely indicates the presence of a second, short-lived open state. We hypothesize that this state results from absorption of a second photon, inducing a parallel low conducting photocycle that underlies the observed substrate inhibition. Parallel photocycles have been implicated in desensitization of green algal ChRs[19,20].

Minimization of light-dependent inactivation results in exceptionally high stationary photocurrents

Next, we aimed to overcome ChRmine desensitization by introducing helix 6 mutations to unleash its potential for life science and medical applications. Mutations in Helix 6 accelerate open to closed state transition in green algal ChRs[18]. We found similar τ_{off} values for ChRmine ($\tau_{off\ (-60\ mV)}$ = 63.5 ± 15.7 ms, n=7), ChRmine T218L ($\tau_{off\ (-60\ mV)}$ = 59.1 ± 21.3 ms, n=7) and ChRmine T218L/S220A ($\tau_{off\ (-60\ mV)}$ = 58.3 ± 12.5 ms, n=7) (Table S1, Fig. S4), whereas ChRmine S220A had slower channel closing kinetics ($\tau_{off\ (-60\ mV)}$ = 152.7 ± 19.8 ms, n=6). Importantly, ChRmine T218L, ChRmine S220A and ChRmine T218L/S220A showed a regular light dependence (hyperbolic, sigmoidal on log-scale, Fig. 1b). Hence, the helix 6 mutants lacked the light-dependent inactivation process found in wild-type ChRmine. In line with this notion, photocurrent desensitization was strongly reduced in the mutants (Fig. 1a, S Fig. S2, Supplementary Table 1): from ChRmine T218L (Stationary-Peak-Ratio: 0.44 ± 0.13, n=18), to ChRmine S220A (Stationary-Peak-Ratio: 0.62 ± 0.14, n=38) and ChRmine T218L/S220A (Stationary-Peak-Ratio: 0.62 ± 0.15, n=21). ChRmine T218L/S220A showed the largest stationary photocurrent density, considerably exceeding current state of the art ChRs (Fig. 1c, d, Supplementary Table 1 and 2) (ChRmine T218L/S220A: 97.6 ± 65.0 pA/pF, n=16 vs. ChRmine WT (21.6 ± 15.8 pA/pF, n=44). We nicknamed it ChReef ("**ChR** that **e**xcites **ef**ficiently") and performed in depth characterization. The channel closing kinetics of ChRmine and ChReef, which carries mutations at non-homologous positions to previously described mutations[18], could be fitted to a mono-exponential function. This indicates that the short-lived second open state does not noticeably contribute to the photocurrent of ChRmine, in line with the suggested role of a parallel photocycle in photocurrent reduction. Next, we determined the single channel conductance of ChReef to 81.9 ± 34.7 fS (n=13, stationary noise analysis) and 100.5 ± 38.0 fS (n=15, non-stationary noise analysis) (Fig. 1f, i), which is statistically indistinguishable to ChRmine. The high-frequency power spectral density component found in ChRmine was not detectable for ChReef (Fig 1f, j), which likely reflects a considerably accelerated transition of the parallel photocycle open state into the main photocycle that results in the minimization of the light-dependent inactivation (Fig. 1 b). The combination of high unitary conductance and minimal photocurrent desensitization qualifies ChReef for efficient and sustained optogenetic stimulation.

Optogenetic stimulation of cardiac tissue

To assess the utility of ChReef for life science applications and future optogenetic therapies, we turned to the cardiac, auditory, and visual systems. We first benchmarked ChReef to ChRmine using cardiomyocyte clusters generated from neonatal mouse hearts following AAV2/9 mediated ChR expression in almost all cardiomyocytes (Figure 2 a,b; 96 ± 1,8% for ChReef and 98 ± 0,5% for ChRmine, N=2 isolations and n=5 coverslips each, unpaired student t-test, $p = 0.11$). In both cases, we achieved reliable optical pacing at 1 Hz with green (510 nm) and red light (625 nm) at irradiances below 100 $\mu W/mm^2$ and 350 $\mu W/mm^2$, respectively (Fig. S7a-c). Higher pacing rates increased the light requirement, in particular for red light for which we found significantly lower pacing thresholds with ChReef at rates of ≥3 Hz (Fig. S7d-f), likely reflecting reduced photocurrent desensitization of ChReef.

Optogenetic cardiac defibrillation of ventricular arrhythmia[21–23] and cardioversion of atrial arrhythmia[22,24,25] are exciting targets for future clinical translational[26]. Here, we compared the efficiency of ChReef and ChRmine for inducing a depolarization block; which is considered the most effective mechanism for optogenetic termination of cardiac arrhythmia[27]. Continuous illumination with green light prevented electrically-evoked contraction of cardiac cell clusters with significantly lower light requirements for ChReef than for ChRmine (Fig. 2c, d). The advantage of using ChReef became still more obvious for red light, where electrically-evoked contraction could be prevented in 14 of 15 ChReef-expressing clusters compared to only 7 of 17

ChRmine-expressing clusters (Fig. 2e, f). This seems highly relevant, as sustained depolarization of the heart muscle upon long wavelength light would be required for future transmural optogenetic termination of arrhythmia[28].

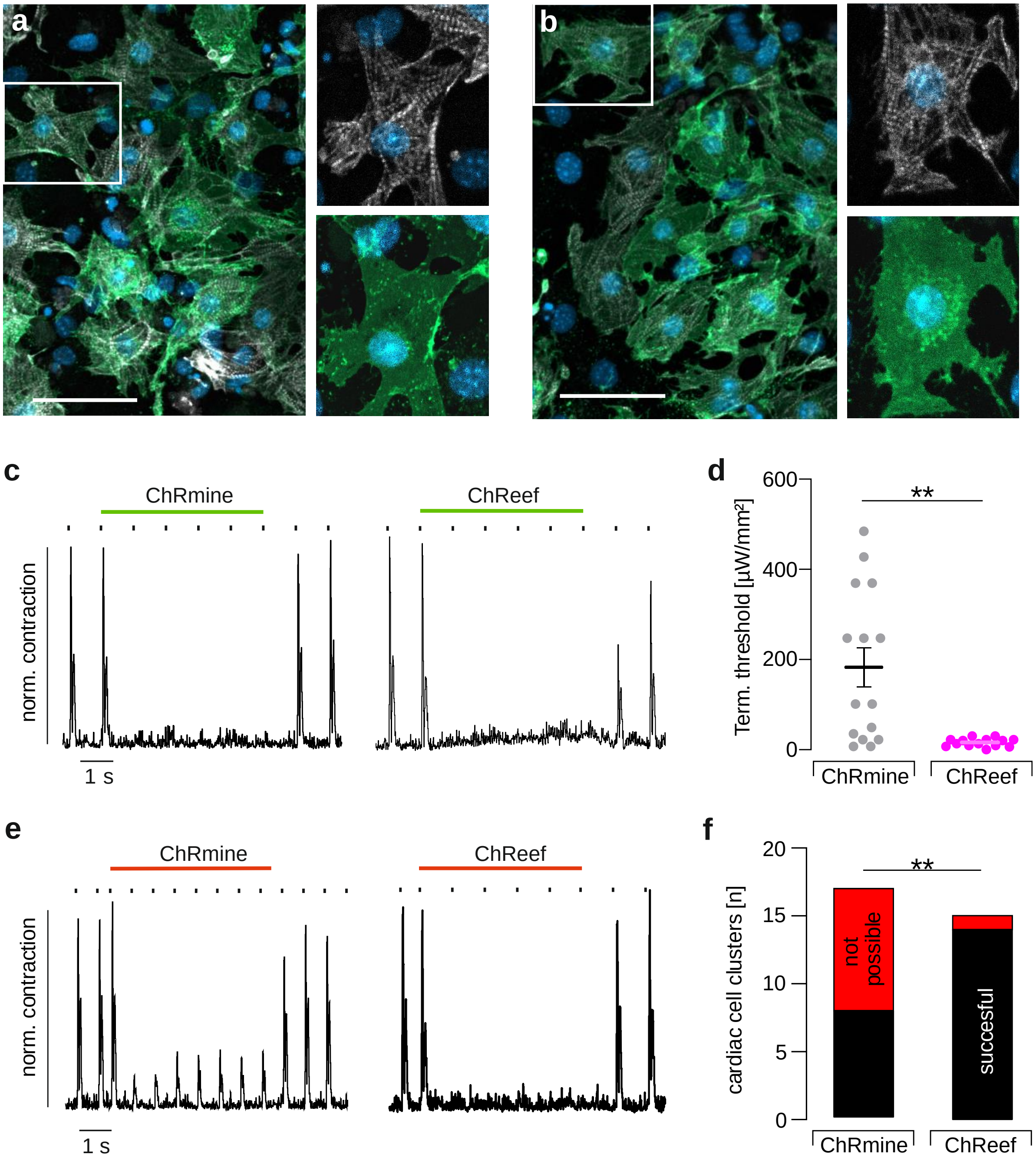

Figure 2. Optical prevention of electrical excitation of cardiac cell clusters. a, Image of a cardiac cell cluster comprising neonatal mouse cardiomyocytes identified by cardiac troponin I staining (white) expressing ChRmine (green) with nuclei stained by Hoechst in blue, bar equals 50 µm. **b**, Image of a cardiac cell cluster comprising neonatal mouse cardiomyocytes identified by cardiac troponin I staining (white) expressing ChReef (green) with nuclei stained by Hoechst in blue, bar equals 50 µm. **c**, Representative traces of contractions of cardiac cell clusters expressing ChRmine (left) and ChReef (right) induced by electrical stimulation (black dots: 0.2 ms biphasic, 45 V) and prevented by continuous illumination with green light (green bar: 510 nm, 5 s, 36 µW/mm^2 for ChRmine and 14 µW/mm^2 for ChReef). **d**, Aggregated data of the required light intensities to inhibit electrical excitation with green light for ChRmine (black) and ChReef (red) expressing cardiac cell clusters. Statistical comparison with a two-sided unpaired student's t test ($p = 0.001$, N = 3 individual isolations and AAV transductions; n = 15 for ChRmine expressing cardiac cell clusters and 14 for ChReef). **e**, Representative traces of contractions of cardiac cell clusters expressing ChRmine (left) and ChReef (right) induced by electrical stimulation (black dots: 0.2 ms biphasic, 45 V) and the effect of continuous illumination with red light (red bar: 625 nm, 5 s, 1 mW/mm^2 for ChRmine and 100 µW/mm^2 for ChReef). Note the still existing contractions during the illumination in the ChRmine example defined as unsuccessful termination. **f**, Aggregated data of the efficiency in preventing contractions with red light (maximal light intensity: 1 mW/mm^2) for ChRmine and ChReef expressing cardiac cell clusters. Statistical analysis was performed with Fisher´s exact contingency test ($p = 0.0028$; N = 3 individual isolations and AAV transductions; n = 17 individual cardiac cell clusters for ChRmine and 15 for ChReef).

Optogenetic vision restoration

Optogenetic restoration of vision is currently being evaluated in clinical trials. In the PIONEER trial, intravitreal injection of AAVs is used to express ChrimsonR cells retinal ganglion cells[2]. A current disadvantage of this approach is that the low light sensitivity requires light-amplifying goggles that employ relatively high light intensities. This limits the dynamic range of optogenetic encoding of visual information and poses a potential risk of phototoxicity for long-term use. Here, we tested the potential of expressing ChReef and ChRmine in retinal ganglion cells for low light optogenetic vision restoration in the rd1 mouse model of retinopathy[29]. AAV-PHP.eB carrying either of the EYFP-tagged ChRs under the control of the human synapsin promotor were intravitreally injected (Fig. 3a). Responses to optogenetic stimulation of the eye to a green LED or an iPad screen positioned close to the mouse eye were recorded by multielectrode arrays inserted into the contralateral primary visual cortex (V1) 3-4 weeks after AAV-administration (Fig. 3b). Single-unit V1 activity could be elicited by full field LED flashes of 200 ms duration at 1 Hz in both ChReef and ChRmine-injected mice (Fig. 3c-f, Fig. S8).

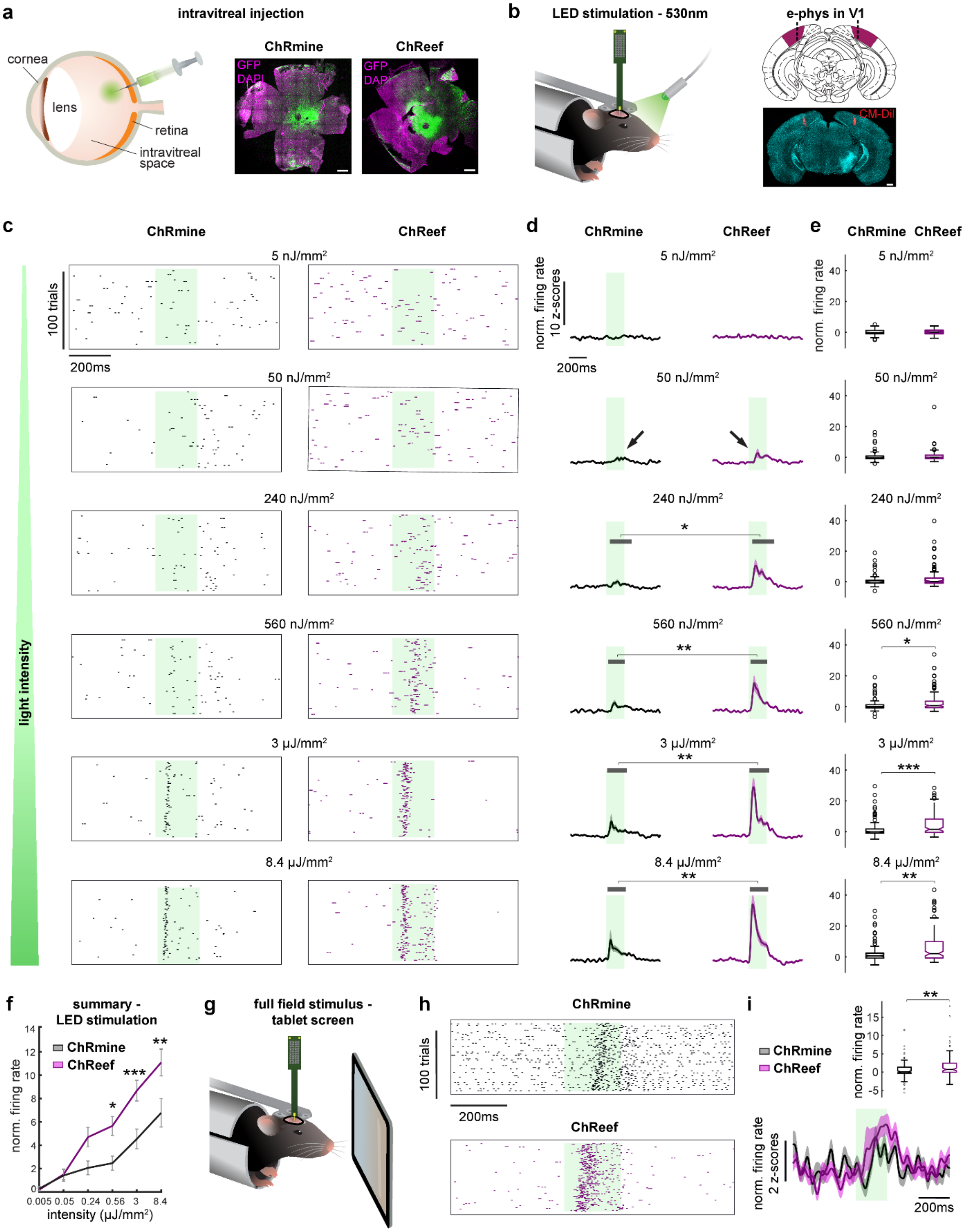

Figure 3. ChReef-mediated vision restoration in rd1 mice has low light requirements

a, Schematic representation of the intravitreal injection approach (left) and expression pattern of both opsins - ChRmine and ChReef – in retinas of rd1 mice after intravitreal injection (right). Scale bar represents 0.5mm. **b**, Vision-restored mice were presented with 200 ms flashes of green light (530 nm) while recording extracellularly in primary visual cortex using 32-channel silicon probes (left). An example brain slice showing the probe's insertion site in V1 (right, electrode track marked by CellTracker™ CM-DiI). Scale bar represents 0.5mm. **c**, Raster plots of two example single units recorded in V1 of ChRmine- and ChReef-injected mice. **d**, Normalized average firing rates of V1 single units in response to varying light intensities. Line and shaded area represent mean ± SEM. Gray lines indicate time clusters of significant difference between the two conditions (Permutation test: see Methods, p (from top to bottom, Bonferroni-Holm corrected) = 0.4062, 0.5021, 0.0162, 0.0042, 0.0048, 0.0066), n = 151 cells in 6 mice (ChRmine), 123 cells in 6 mice (ChReef)). **e**, Average normalized firing rate during the stimulus window for the same neurons as in d (Mann-Whitney-U-test, p (from top to bottom, Bonferroni-Holm corrected) = 0.2349, 0.1468, 0.0671, 0.0451, 0.0001, 0.0049). Central line indicates median, box includes data from 25th to 75th percentile and the whiskers span the most extreme data points not considering outliers (empty circles). **f** Average normalized firing rate during the stimulus window as in **e**. Error bars represent ± SEM. **g**, Schematic depicts the experimental approach for **h-i**. In contrast to green LED flashes, here we employed an iPad screen to present white, full-field flashes of 200 ms. **h**, Raster plots of two example V1 neurons are shown. **i**, Normalized firing rates of V1 single units in response to the iPad-delivered full-field flash, n = 90 cells in 5 mice (ChRmine), 110 cells in 6 mice (ChReef). Line and shaded area represent mean ± SEM. Inset shows the average normalized firing rate during the stimulus for the same cells (Mann-Whitney-U-test, p = 0.0093).

For both ChReef and ChRmine, we observed cells that responded at light intensities as low as 0.25 µW/mm^2 (50 nJ/mm^2, Fig. 3d arrows and Fig. S8a), which is around the light intensities observed in indoor settings[30] demonstrating high light sensitivity conferred to retinal ganglion cells by both ChRs. Importantly, ChReef injected animals showed stronger and more sustained V1 activity compared to ChRmine, especially at low light intensities (Fig. 3c-f, Fig. S8). In further support of high sensitivity vision restoration, full-field stimuli presented to the eye from an iPad screen also elicited V1 activity in both ChRmine and ChReef injected mice (Fig. 3g-i). Again, V1 activity was stronger and more sustained in ChReef compared to ChRmine expressing animals

(Fig. 3i). This indicates that ChReef enables the use of computer screens for versatile visual stimulation in vision research and for restoring vision in blind patients at lower light intensities.

Optogenetic stimulation of the auditory periphery

Optogenetics also promises to transform the restoration of hearing by cochlear implants (CIs)[4,5] to achieve near natural hearing. Electrical CIs (eCIs) used in currently ~1 Mio otherwise deaf users, bypass dysfunctional or lost sensory hair cells by direct electrical stimulation of spiral ganglion neurons (SGNs). eCIs typically enable 1-to-1 conversation in a quiet environment, yet, understanding speech in background noise remains a major unmet clinical need[31]. Optogenetic SGN stimulation could transform CI hearing as light, different from current, can be confined in space. Hence, optical CI (oCI) provide near natural spectral selectivity of optogenetic SGN stimulation, outperforming the eCI[32,33]. One of the challenges for clinical translation of the oCI is the increased power budget that results from upscaling the number of stimulation channels (oCI: 64 planned vs. eCI: 12-24) and the higher energy required per stimulus[4,5]. Using the ChRs currently available, pulse energy thresholds for optogenetic SGN stimulation range from 1.500 nJ to 12.000 nJ[5] compared to 50 nJ for eCI[34]. Reducing the required pulse energy by greater light efficiency of optogenetic SGN stimulation remains a key objective *en route* to clinical translation of the oCI. Here, we employed physiological analysis of the auditory system in mice and gerbils for assessing the potential of ChReef for energy-efficient optogenetic SGN stimulation. First, we studied optogenetic stimulation at the levels of SGN population as well as of individual SGNs and cochlear nucleus neurons in mice 3-10 weeks after early postnatal intracochlear injection of AAV2/9 carrying ChReef or ChRmine. Expression of both ChR variants under the control of the human synapsin promotor was found in approximately 75% of the SGNs (Fig. 4b, Fig. S9).

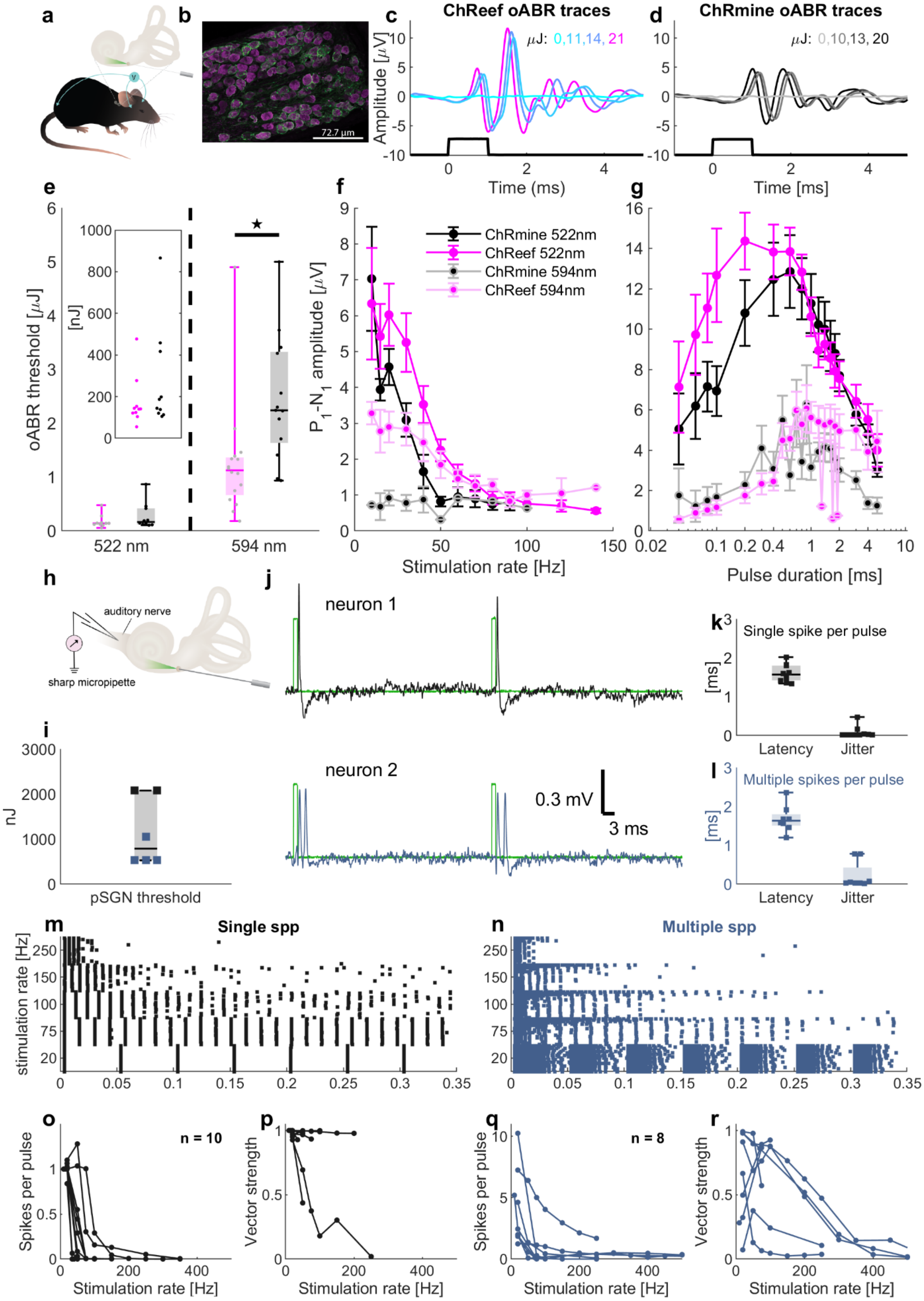
a
b
72.7 µm
c
ChReef oABR traces
µJ: 0,11,14, 21
Amplitude [µV]
10
5
0
-5
-10
0
2
4
Time (ms)
d
ChRmine oABR traces
µJ: 0,10,13, 20
Time [ms]
e
oABR threshold [µJ]
0
1
2
3
4
5
6
[nJ]
1000
800
600
400
200
0
★
522 nm
594 nm
f
P1-N1 amplitude [µV]
9
8
7
6
5
4
3
2
1
0
ChRmine 522nm
ChReef 522nm
ChRmine 594nm
ChReef 594nm
0
50
100
150
Stimulation rate [Hz]
g
16
14
12
10
8
6
4
2
0
0.02
0.1
0.2
0.4
1
2
4
10
Pulse duration [ms]
h
auditory nerve
sharp micropipette
i
3000
2000
1000
0
nJ
pSGN threshold
j
neuron 1
neuron 2
0.3 mV
3 ms
k
Single spike per pulse
[ms]
3
2
1
0
Latency
Jitter
l
Multiple spikes per pulse
[ms]
3
2
1
0
Latency
Jitter
m
Single spp
stimulation rate [Hz]
250
150
100
75
20
0
0.05
0.1
0.15
0.2
0.25
0.3
0.35
n
Multiple spp
250
150
100
75
20
0
0.05
0.1
0.15
0.2
0.25
0.3
0.35
o
Spikes per pulse
n = 10
1
0.5
0
0
200
400
Stimulation rate [Hz]
p
Vector strength
1
0.5
0
0
200
400
Stimulation rate [Hz]
q
Spikes per pulse
n = 8
10
5
0
0
200
400
Stimulation rate [Hz]
r
Vector strength
1
0.5
0
0
200
400
Stimulation rate [Hz]

Figure 4. ChReef-mediated optogenetic stimulation of the mouse auditory nerve has low light requirements and acceptable temporal fidelity. a, Schematic representation of optical auditory brainstem recordings (oABR): a laser-coupled fiber was inserted into the round window. **b**, Mid-modiolar cochlear slice at the apical turn displaying SGN transduction (stained for anti-GFP in green and anti-Parvalbumin in magenta). **c, d**, oABRs driven with varying radiant flux (1 ms pulses at 10 Hz, colors code the radiant flux in mW) for exemplary mice injected with AAV2/9-hSyn-ChReef-ES-EYFP-TS (**c**) or AAV2/9-hSyn-ChRmine-ES-EYFP-TS (**d**). **e**, Energy threshold of oABRs for ChReef (magenta) and ChRmine (black) using both 522 nm (left panel, inset shows data on separate axis) and 594 nm (right panel) light: center line: mean, box: SD, error bars: minima and maxima, n = 17 mice for ChReef and n = 16 mice for ChRmine (*p = 0.004, t-test). **f**, P1-N1 amplitudes of oABRs at varying repetition rates using 1 ms, 10 mW pulses (mean ± SD) with 522 nm (ChReef: magenta; ChRmine: black) and 594 nm (ChReef: pale magenta; ChRmine: grey). **g**, P1-N1 amplitudes of oABRs for varying pulse durations using ~10 mW pulses at 10 Hz (mean ± SD). **h**, Juxtacellular recordings from putative SGNs upon ChReef-mediated optogenetic stimulation by 1 ms, 522 nm light pulses. **i**, Energy threshold of individual SGNs (criteria: spike per pulse> 0.005, vector strength > 0.3) **j**, Exemplary responses of SGNs to 1ms, ~6mW pulses at 20Hz illustrating two SGN response categories: single spike responding (<=1.1spikes per pulse, black) and multiple spike responding SGNs (>1.1 spike per pulse, blue). **k-**l, Median of first spike latency and first spike jitter. **m-n**, Exemplary raster plots (SGNs of **i, j**) showing responses to 350 ms-long trains of laser pulses at varying stimulation rates. **o-r**, Spike probability and vectors strength of single spike and multiple spike responding SGNs at varying stimulation rates.

Optically evoked auditory brainstem responses (oABR, Fig. 4a-g) were elicited in all mice upon stimulation with green (522 nm, optimal excitation) and long-wavelength (594 nm) light delivered by a laser-coupled optical fiber to the cochlea. oABR energy thresholds of ChReef expressing mice (Fig. 4e, 522 nm: 170 ± 120 nJ, *n* = 10 vs. 270 ± 240 nJ, *n* = 10 for ChRmine; p = 0.127, *t-test*) were almost a magnitude lower than the previously reported lowest threshold found with f-Chrimson[18] (1.500 ± 100 nJ, p < 0.0005). ChReef oABR thresholds were significantly lower than those for ChRmine for longer wavelength light (594 nm, 1.250 ± 1070 nJ, *n*=16 vs. 2.450 ± 1.160 nJ, *n* = 13; p = 0.004, t-test) which is relevant when considering future clinical oCI. The optically evoked SGN compound action potential (P1-N1 oABR amplitude) grew with increasing radiant flux (Fig. S10) without obvious saturation promising a broad dynamic range of ChReef and ChRmine-mediated optogenetic sound encoding. To evaluate the temporal fidelity of optogenetic SGN stimulation, we recorded oABRs in response to green and orange light pulses at different stimulation rates (1 ms, 10 mW, Fig. 4f). oABR amplitudes declined with increasing stimulation rate, whereby ChReef showed detectable oABRs to stimulation rates beyond 100 Hz compared to 50 Hz for ChRmine. Both ChReef and ChRmine enabled oABRs in response to 20 µs-long durations of green light pulses whereby the duration eliciting the maximal P1-N1 oABR amplitude was shorter for ChReef (Fig. 4g: 200 µs for ChReef vs. 600 µs).

To further scrutinize the ChReef-mediated optogenetic stimulation of the auditory nerve, we turned to stereotactic *in vivo* recordings from single putative SGNs (here forth coined SGNs) upon green light stimulation from an optical fiber inserted into the round window of the mouse cochlea[18,35,36] (Fig. 4h). Approximately two-thirds of the SGNs responded to optogenetic stimulation (Fig. 4h-j, 1ms of 522 nm light at 6 mW radiant flux and 20 Hz repetition rate) with a single spike and the other third with multiple spikes (mostly 2-3 but some with more tonic discharge). This is reminiscent of responses of CatCh-expressing SGNs in Mongolian gerbils[37]. Single SGN energy thresholds (Fig. 4i, < 2.000 nJ) tended to be higher than oABR thresholds but still much lower than all previously reported values (>6.000 nJ, for f-Chrimson, vf-Chrimson and Chronos[36,38]. First spike latency and first spike latency jitter were comparable among the two SGN groups (Fig. 4k, l). Next, we studied spike probability and spike synchronization with the stimulus as a function of stimulation rate for both SGN groups (Fig. 4o-r). Many SGNs failed to reliably follow stimulus rates beyond 50 Hz which seems in keeping with the oABR findings (Fig. 4f), but a number of multiple spike responding SGNs showed temporal precise coding of light stimuli for rates > 100 Hz. Both, recordings of oABRs and single SGNs entailed optogenetic stimulation over several hours without obvious loss of responsiveness along the experiment. Finally, we performed patch-clamp recordings of optogenetically (green-light) driven synaptic transmission from ChReef-expressing SGNs to bushy cells in acute slices of the cochlear nucleus (Fig. S11). Excitatory postsynaptic recordings were reliably evoked for rates of stimulation ≤50 Hz.

To assess the representation of ChReef-mediated SGN stimulation in the central nervous system, we performed multielectrode array recordings of multi-unit activity in the auditory midbrain (inferior colliculus, IC[32], Fig. 5a, Fig. S13) in response to green light (522 nm) SGN stimulation in Mongolian gerbils. Following postnatal cochlear injection of AAV-PHP.S carrying ChReef under the control of the human synapsin promotor (Fig. S12), we recorded ChReef-mediated oABRs and moved on to IC recordings in gerbils with low oABR thresholds (152 ± 64 nJ, *n*=5, Fig. S14). The energy threshold for 1 ms light stimuli to elicit multi-unit activity in the IC of these gerbils amounted to 120 ± 70 nJ (*n* = 6, Fig. 5c, d' = 1). The evoked multi-unit activity occurred over a similar time window as previously reported for CatCh-mediated SGN stimulation (2.7-24.2 ms for ChReef vs. 2.2-24.5 ms for CatCh[32]). The firing rate tended to plateau around 50 Hz of stimulation (Fig. 5j), until which decent synchronization of firing with the stimulus was observed (Fig. 5i, vector strength: ~0.5). Synchrony of firing degraded at higher stimulation rates (vector strength: ~0.2 at 100 Hz). Both light requirements and temporal fidelity of IC activity are consistent with the observed ChReef-mediated SGN stimulation (Fig. 4 , Fig. S11). Together, these auditory systems data demonstrate nano-Joule and sustained optogenetic stimulation of the auditory pathway capitalizing on the higher single-channel conductance, longer open times, and sustained photocurrents of ChReef.

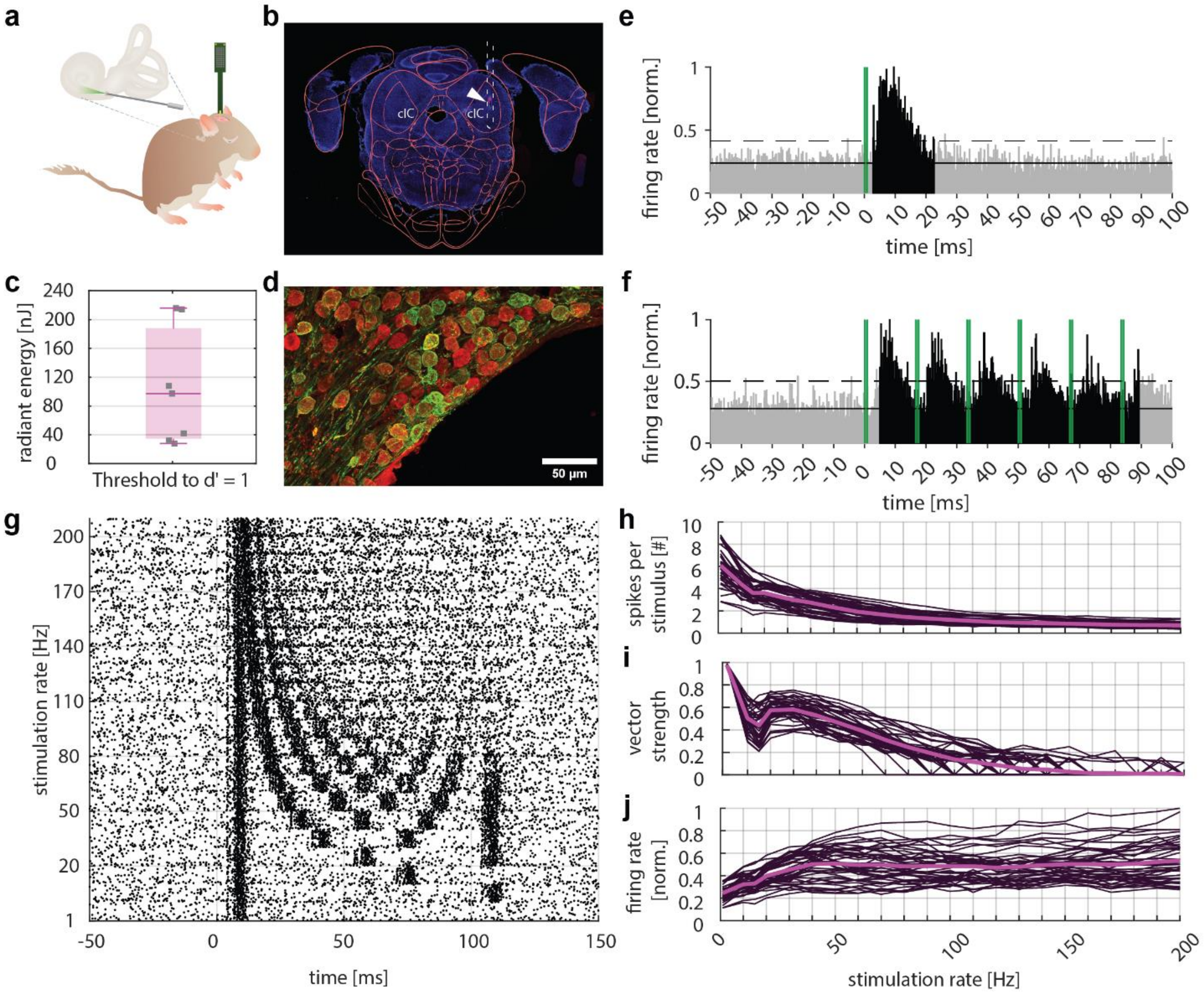

Figure 5: Characterizing the optogenetic activation of the auditory pathway by means of inferior colliculus recordings in Mongolian gerbils

a, Schematic describing experimental setup. **b**, Coronal section of a gerbil brain indicating placement of multi-unit electrode, stained with DiL. **c**, Neuronal thresholds computed as level eliciting a d' of 1. Gray squares indicate lowest radiant energy measured from using green light for each animal that could generate a response allowing for the d' criterion indicated to be met. **d,** Mid-modiolar section displaying SGN transduction (stained for anti-GFP in green and anti-Parvalbumin in red) **e,f**, Peri-Stimulus Time Histogram (PSTH) computing spike rates in bins of 0.2 ms recorded from stimulating at ~1 mW with an optical fiber emitting green light (522 nm, n = 6, **e**) and pulsing at 60Hz (n = 6, **f**) normalized to the highest spike rate across animals. Green lines indicate stimulus timing. Dashed horizontal lines indicate 3x mean absolute deviation (MAD) used for thresholding and bins reaching threshold condition are highlighted in black. **g**, Exemplary spike raster computed from stimulating at 1 mW across different stimulation rates used for each of the 30 repetitions. Stimulus used were 100 ms pulse trains of 1 ms light pulses delivered at various stimulation rates. **h,i,j**, Individual traces computed across all animals and all responsive channels demonstrating spikes/stimulus, vector strength and firing rates recorded and normalized to highest firing rate computed respectively. Average shown in bold magenta lines.

Discussion

ChReef is a new optogenetic actuator for sustained optogenetic control of excitable cells enabling firing rates of up to 50-100 Hz with nano-Joule light requirements which we expect to facilitate a wide range of optogenetic applications. Combining good membrane targeting, higher single channel conductance, moderate open times, and low photocurrent desensitization, ChReef enabled breakthroughs in three different optogenetic applications: Efficient red-light optogenetic conduction block of cardiomyocytes, optogenetic vision restoration at low light intensities, and lowering the energy threshold for optogenetic activation of the auditory pathway by one order of magnitude. The closing kinetics of ChReef (~30 ms deactivation time constant) provide a good match to the temporal fidelity required for optogenetic control of cardiomyocytes and retinal ganglion cells. For the auditory system, the temporal fidelity of SGN stimulation was inferior to that observed with ultrafast ChRs such as f-Chrimson, vf-Chrimson and Chronos (deactivation time constants of 3, 1.5, and <1 ms at body temperature, respectively)[14,18,36,38]. Current eCI coding strategies employ high stimulation rates (~1 kHz) for sampling the envelope of the sound signal. However, good speech understanding was obtained at much lower rates (from 20 Hz[39]) in the range achievable by ChReef-mediated SGN stimulation (up to ~100 Hz). Nonetheless, future efforts should aim for generating ChReef variants with faster closing kinetics to enhance the temporal fidelity of optogenetic stimulation and to further shift the absorption to longer wavelengths for better alignment with red-light laserdiode-based medical devices such as optical cochlear implants.

Material and Methods

ChR variant generation

The humanized DNA sequence, coding for *Rl*CCR1-309 (*Rhodomonas lens ChR*, also called ChRmine, accession number: MN194599[10,40]), C-terminally fused to TS-EYFP-ES was cloned into the mammalian expression vector pcDNA3.1 (−) (Invitrogen, Carlsbad, USA). The previously described targeting sequences of the inward rectifying potassium channel Kir2.1 (TS and ES) were employed for optimized plasma membrane expression[8,13,14]. The mutations T218L and S220A were introduced into ChRmine by site-directed mutagenesis using the primers shown in Supplementary Table 3.

The pcDNA3.1(-) derivatives carrying the humanized DNA sequences of Chronos-EYFP (*Stigeoclonium helveticum* ChR, accession number: KF992040[41]), ChR2-EYFP (C-terminally truncated variant Chop2-315 of ChR2 from *Chlamydomonas reinhardtii*, accession number: AF461397[42]), CatCh-EYFP (ChR2 L132C), Chrimson-EYFP (*Chlamydomonas noctigama* ChR, accession number: KF992060[41]) and f-Chrimson-EYFP (Chrimson Y261F/S267M[36]) were kindly provided by Ernst Bamberg (MPI of Biophysics). The previously described mutation T159C[18] was introduced into ChR2 by site-directed mutagenesis (sequence of forward primer: 5´-TCCGACATCGGCTGTATCGTATGGGG-3´, sequence of reverse primer: 5´-CCCCATACGATACAGCCGATGTCGGA-3´).

***In vitro* measurements**

Cell culture and transfection

The manual patch-clamp recordings of ChR variants were conducted in the neuroma glioblastoma cell line NG108-15 (ATCC, HB-12377TM, Manassas, USA) cultured in Dulbecco's Modified Eagle Medium (DMEM, Sigma, St. Louis, USA) supplemented with 10 % fetal calf serum (Sigma, St. Louis, USA) and 1 % penicillin/streptomycin (Sigma, St. Louis, USA) (supplemented DMEM: DMEM$^+$) at 37 °C and 5 % CO_2. Cells were seeded on 24-well plates one day prior to transfection by Lipofectamine with pcDNA3.1(-) derivatives carrying the aforementioned ChR variants at a NG108-15 cell confluency of 50-70 %. For each well, a transfection mix of 100 µl DMEM, 3 µl Lipofectamine LTX (Invitrogen, Carlsbad, USA) and 500 ng of the pcDNA3.1(-) derivatives was prepared and added to a well with 400 µl of DMEM$^+$. Twenty-four hours after transfection the medium was exchanged against 500 µl DMEM$^+$ supplemented with 1 µM all-trans retinal.

For automated patch-clamp recordings, HEK293T cells (DSMZ, Braunschweig, Germany) were seeded in a T75 culture flask and allowed to grow for one day before transfection. The cells were seeded at a density of 1.2 million cells in 15 ml of DMEM$^+$. Immediately prior to transfection, the media was replaced with 12 mL of OptiMEM (ThermoFisher, Waltham, Massachusetts, U.S.) with 1.25 µM all-trans-retinal (Sigma, St. Louis, MO, U.S.). For transfection, 19.5 µg of plasmid DNA and 78.1 µg of polyethyleneimine (PEI, Polysciences, Warrington, PA, U.S.) were separately dissolved in 1.5 ml of OptiMEM (ThermoFisher, Waltham, Massachusetts, U.S.) each. The DNA and PEI solutions were then combined and incubated for 15 minutes at room temperature. The resulting DNA/PEI mix was added to the cells and incubated at 37°C and 5% CO_2 for 4 hours. After transfection, the media in the flask was changed back to DMEM$^+$ supplemented with 1 µM all-trans-retinal. The cells were then incubated at 37°C and 5% CO_2 for 40 hours prior to the automated patch-clamp experiment.

Manual patch-clamp recordings and data analysis

The electrophysiological characterization of the ChR variants was conducted by whole cell patch-clamp recordings of transiently transfected NG108-15 cells at membrane potential of -60 mV, if not stated differently. Cells were patched two days after transfection under voltage-clamp conditions using the Axopatch 200B amplifier (Axon Instruments, Union City, USA) and the DigiData1322A interface (Axon Instruments, Union City, USA). Patch pipettes with a resistance of 2-6 MΩ were fabricated from thin-walled borosilicate glass on a horizontal puller (Model P-1000, Sutter Instruments, Novato, USA). The series resistance was <15 MΩ. The bath solution contained 140mM NaCl, 2mM $CaCl_2$, 2mM $MgCl_2$, 10mM HEPES, pH 7.4; and the pipette solution contained 110mM NaCl, 2mM $MgCl_2$, 10mM EGTA, 10mM HEPES, pH 7.4. All recordings were performed at room temperature (20°C). Light pulses were applied by a fast computer-controlled shutter (Uniblitz LS6ZM2, Vincent Associates, Rochester, USA) using diode-pumped solid-state lasers focused into an optic fiber (d=400 µm). The open-source statistic software "R" as well as Origin 9.0 (OriginLab, Inc., Northampton, MA, USA) and GraphPad Prism (GraphPad Software, La Jolla, CA, USA) were employed for data analysis.

The photocurrents of the ChRmine variants were measured in response to green light pulses (λ=532 nm) of varying duration with a saturating intensity of 23 mW/mm^2. The photocurrents of Chronos, Catch and ChR2 T159C were measured upon the application of blue light pulses (λ=473 nm) of varying duration with a saturating intensity of 31 mW/mm^2. The stationary current densities ($J_{-60\ mV}$) of the ChRmine variants were calculated as the quotient of the mean stationary current upon stimulation with a 2 s light pulse and the capacitance of the cell. The stationary current densities ($J_{-60\ mV}$) of Chronos, Catch and ChR2 T159C were calculated as the quotient of the mean stationary current upon stimulation with a 0.5 s light pulse and the capacitance of the cell. To avoid an experimental bias, cells were chosen for the recordings independent of the brightness of their fluorescent signal.

The stationary-peak-ratio of the photocurrents of the ChRmine variants was calculated as the quotient of the mean stationary current upon stimulation with a 2 s light pulse and the peak current. The peak recovery of the ChRmine variants was assessed by photocurrent recordings upon illumination with two subsequent 3 s light pulses with a varying time between the light pulses (Δt between pulses, ms, ranging from 50 to 3350 ms). Peak recovery was calculated as the quotient of the difference between the peak and stationary current of pulse two (I_{p2}-I_{s2}) and peak and stationary current of pulse one (I_{p1}-I_{s1}) in %. The time constant of the peak recovery ($\tau_{peak\text{-}recovery}$) was determined by a fit of the quotient of the difference between the peak and stationary currents of two subsequent 3s light pulses at saturating intensity to a monoexponential function.

The light intensity dependence of the stationary photocurrent of the ChRmine variants was investigated by photocurrent measurements upon illumination with 2 s light pulses (λ=532 nm). The EC_{50} values were determined by hyperbolic fitting. For ChRmine wt the fitting range was thereby restricted to the range, which could be approximated by a hyperbolic function. The light intensity dependence of ChRmine wt was furthermore fitted to an equation corresponding to a steady state minimal kinetic model describing a substrate inhibition of the partial type [15]:

$$I = I_{max}\frac{\left(1+\frac{E}{K_i}R_c\right)E}{\left(1+\frac{E}{K_i}\right)E+K_a} \qquad \text{[Equation 1]}$$

I: stationary photocurrent, I_{max}: maximal stationary photocurrent if $K_i \rightarrow \infty$, E: irradiance, R_c: effective ratio of single channel currents (i_1/i_2), K_a: effective equilibrium constant for light dependent closed (C) to open transitions (O1), K_i: effective equilibrium constant for light dependent transitions between open states (O1/O2). The light intensity dependence shown in Figure 1 was fitted with the following parameters: K_a=0.021±0.005, K_i=0.062±0.029, R_c=0.47±0.05. Although the informative value of the fitted parameters is limited due to the absence of a more detailed description of the ChRmine photocycle, which could serve as a basis for a precise kinetic model, the fit demonstrates that the light intensity dependence of the stationary photocurrent of ChRmine resembles a substrate inhibition of the partial type.

The τ_{off} values of all shown ChR variants were determined by a fit of the decaying photocurrent elicited in response to a 3 ms light pulse to a monoexponential function. In order to investigate the dependence of the off-kinetics on the membrane potential τ_{off} values were determined at membrane potentials ranging from -120 mV to +60 mV.

The action spectra of the ChRmine variants were determined by peak current recordings in response to ns-light-pulses of wavelengths ranging from 430 to 590 nm with pulse energies at the different wavelengths set to equal photon counts of $5*10^{18}$ photons/m^2 using the Opolette 355 tunable laser system (Opotek Inc, Carlsbad, USA).

Automated patch-clamp recordings and data analysis

The automated patch-clamp recordings were done using Syncropatch 384 (Nanion, Munich, Germany) equipped with prototype illumination units. The Syncropatch 384 robot was operated using the Biomek v2.1 software. The data was acquired using the PatchControl v2.1 software. The HEK293T cells that were transfected were washed twice with DPBS (ThermoFisher, Waltham, Massachusetts, U.S.) and then treated with 3 ml of TrypLE (ThermoFisher, Waltham, Massachusetts, U.S.) at 37°C for 7 minutes. After the TrypLE treatment, 3 ml of standard external solution was added to the cells and incubated at 4°C for 5 minutes. The standard external solution was composed of 140 mM NaCl, 4 mM KCl, 2 mM $CaCl_2$, 1 mM $MgCl_2$, and 10 mM HEPES, with pH adjusted to 7.4 using NaOH. The osmolarity of the solution was set to 298 mOsm by adjusting the concentration of glucose. The cells were then resuspended by pipetting and centrifuged at 200 g for 10 minutes, and the supernatant was discarded. Finally, the cells were resuspended in 10 mL of Standard External Solution.

To begin, the S-type chip (Nanion, Munich, Germany) was filled with 80 µl per well of Divalent-Free solution, and the chamber's bottom was subsequently filled with Internal solution. The Divalent Free solution contained 140 mM NaCl, 4 mM KCl, and 10 mM HEPES, with pH adjusted to 7.4 using NaOH. The osmolarity of the solution was set to 289 mOsm by adjusting the concentration of glucose. The Internal solution was composed of 10 mM NaCl, 10 mM KCl, 110 mM KF, 10 mM HEPES, and 10 mM EGTA, with pH adjusted to 7.2 using KOH. The osmolarity of the solution was set to 285 mOsm by adjusting the concentration of glucose. Next, 20 µl per well of solution was removed, and 20 µl per well of detached cells were introduced to the chip. The cells were then captured by a suction pulse of -200 mbar for 5 s, followed by consecutive suction pulses of -50 mbar for 1 min. Subsequently, the voltage was decreased incrementally from 0 mV to -100 mV in steps of 25 mV while maintaining the cells under a pressure of -50 mbar. After this, 20 µl per well of solution was removed from the chip, and 40 µl per well of seal enhancer solution was added. The seal enhancer solution contained 130 mM NaCl, 4 mM KCl, 10 mM $CaCl_2$, 1 mM $MgCl_2$, and 10 mM HEPES, with pH adjusted to 7.4 using NaOH. The osmolarity of the solution was set to 302 mOsm by adjusting the concentration of glucose. The chip then underwent three wash steps, during which 40 µl of solution was removed from each well and replaced with 40 µl per well of standard external solution. After the second wash step, two suction pulses of -220 mbar were applied for 2 s each to establish a whole-cell configuration. After completing all of the procedures described, the remaining volume of solution in the wells was 100 µl. To illuminate the cells during the planar patch clamp experiment, a specialized illumination unit was utilized. The unit consists of 96 LEDs (Lumileds Luxeon Z, Schiphol, Haarlemmermeer, The Netherlands) that are coupled to light fibers. During the experiment, the end of the fiber is submerged under the solution and positioned 7 mm from the cell being measured. The illumination unit with λ_{max} = 530 nm (LXZ1-PM01) LEDs was used in all planar patch clamp experiments with ChReef and ChRmine, the unit with λ_{max} = 470 nm LEDs (LXZ1-PB01) was used in experiments with CatCh. To regulate the intensity of light used in each measurement, the forward current of the illumination unit was adjusted. The intensity was measured directly at the output of the light fibers using a bolometer (Coherent OP-2 VIS, Santa Clara, California, U.S.). The intensity of light was specified for each type of measurement.

The data collection for the noise analyses of both types started with measurement of photocurrent dependence on the membrane voltage (IV curve). The range of voltages was from -120 mV to 60 mV with equidistant 20 mV steps. Each sweep was separated into three consecutive steps, with 2 s in the dark, 2 s under the illumination of a saturating intensity for the stationary photocurrents of the measured ChRs (4 mW/mm^2 for ChReef and ChRmine; 6 mW/mm^2 for CatCh) and 1 s in the dark. This data was used to calculate the reversal potentials, which were used to determine the electrochemical potentials on the membranes. This step was followed by different protocols and data treatment procedures for stationary and non-stationary analyses. The data treatment encompassed a thorough selection of recordings that met our strict quality control criteria, followed by the processing of the selected raw traces using our proprietary Python library and custom scripts developed in-house.

For stationary analyses, all cells were held at a voltage of -100 mV or -60 mV. 40 consecutive pairs of sweeps, 6.5 s long each, were recorded at a sampling rate of 20 kHz. Each pair of sweeps was followed by 25 s of non-recorded waiting time in the dark. The first sweep of each pair had a 6-second illumination pulse at an intensity of 0.4 mW/mm^2 (0.6 mW/mm^2 for CatCh), and the second sweep was recorded under dark conditions.

Sweeps suitable for stationary noise analysis were selected based on the following criteria. Basic parameters of the seals were assessed for each sweep, and only sweeps with a seal resistance over 1 GΩ, a membrane capacitance lower than 50 pF, and a series resistance below 20 MΩ were used for further analysis. The parameters of the dark noise were then assessed using parts recorded under the dark conditions for the sweeps with data recorded under illumination conditions. Sweeps with a root mean square deviation (IRMS) of dark currents over 5.5 pA were disregarded. The stability of the noise was assessed by dividing the dark part of the current into 100 pieces, calculating IRMS in all of them, and disregarding sweeps with a standard deviation of IRMS over 0.3 pA. The recorded sweeps were grouped back into pairs of consecutive traces that were recorded under light and dark conditions. Only those pairs with stationary photocurrents over 200 pA during the interval from 2 to 6 s after turning on the illumination were considered. Cells that had four or more pairs of traces remaining after applying all of the aforementioned quality control criteria were selected for stationary noise analysis. For each pair, the interval from 2 to 6 s was taken. The sweep recorded under the light conditions was fitted to a double exponential function, and the resulting fit was subtracted from the sweep. A mean current was subtracted from the sweep recorded in the dark. After these corrections, the power spectral density (PSD) was calculated for both sweeps. The differences between the PSD under the light and dark conditions were determined and then averaged for each cell. The averaged difference PSDs were then fitted to the single Lorentzian function in a range from 2.5 to 25 Hz. This allowed for the determination of the corner frequency and the difference PSD at 0 Hz (f_c and S_0 correspondingly as in eq. 2). Open probabilities of the channels (P_o) were then determined for each cell, taking into consideration their relation (eq. 3) to corner frequency and off kinetics (where τ_{off} was determined from the single exponential fit of the photocurrent decrease after turning off the light). Only cells whose difference PSD met the criteria of $1 \text{ Hz} < f_c < 15 \text{ Hz}$ and $0 < P_o < 1$ were considered in the determination of the single channel conductance values.

$$S(f) = \frac{S_0}{1 + \left(\frac{f}{f_c}\right)^2} \qquad \text{[Equation 2]}$$

$$1 - P_o = \frac{1}{2\,\pi f_c \tau_{off}} \qquad \text{[Equation 3]}$$

The variances σ^2 of the noise associated with the opening and closing of the ChRs were determined by utilizing the obtained values of f_c and S_0 (eq. 4). The unitary photocurrents were subsequently calculated by applying the relation between the mean and variance in the binomial distribution (eq. 5) to the mean net stationary current I and σ^2. Afterwards, the unitary photocurrents were converted to single channel conductances by dividing them by the electrochemical potential gradient.

$$\sigma^2 = \frac{\pi f_c S_0}{2} \qquad \text{[Equation 4]}$$

$$i = \frac{\sigma^2}{I\,(1 - P_o)} \qquad \text{[Equation 5]}$$

In the non-stationary analysis, 300 sweeps were recorded for each cell at the holding voltage of -100 mV or -60 mV. At -100 mV each sweep had a 5 ms illumination step at an intensity of 14 mW/mm^2 forward current so that recordings are done close to single turnover conditions, preventing protein from going to the putative second open state upon absorption of a second photon. At -60 mV each sweep had an illumination step of 150 ms at an intensity of 0.4 mW/mm^2. After each illumination step the dark currents were recorded for 5 s.

The non-stationary noise analysis involved several steps to select the suitable sweeps for analysis. Firstly, basic parameters of the seals were assessed, and only those sweeps that met the following criteria were used: seal resistance over 1 GΩ, membrane capacitance lower than 50 pF, and series resistance below 20 MΩ. Sweeps with root mean square deviation (IRMS) of dark currents over 4.5 pA were disregarded. Only cells with a peak photocurrent over 500 pA (over

100 pA for -60 mV traces) were considered. To minimize possible unwanted effects of the photocurrent rundown, only the sets of at least 50 consecutive recordings (25 recordings for -60 mV traces) with negligible rundown of the peak photocurrent (lower than 1 pA/sweep) were considered and the variance of the photocurrent was determined as a half of the average of the squared differences between pairs of consecutive recordings. The dependence of the variance on the photocurrent value was then fitted linearly to determine the unitary photocurrent as a proportionality factor (eq. 6) and the background current variance as the free term (σ_b^2, squared IRMS at photocurrent of 0 pA). Finally, any cells that had linear fits indicating σ_b smaller than 4 pA were excluded from the analysis, since none of the recordings showed such a low IRMS value based on its direct calculation in the dark current. The remaining cells were used to compute the single channel conductance.

$$\sigma^2 = P_o(1-P_o)Ni^2 + \sigma_b^2 \approx P_oNi^2 + \sigma_b^2 = I \cdot i + \sigma_b^2 \qquad \text{[Equation 6]}$$

***Ex vivo* and *in vivo* experiments – General**

rAAV purification and cloning of constructs for *ex vivo* and *in vivo* experiments

Viral vector purification procedure was performed as previously published[14] and an extensive description is available in[43]. In brief, triple transfection of HEK-293T cells was performed using the pHelper plasmid (TaKaRa, USA), trans-plasmid with either the AAV2/9, PHP.eB or PhP.S capsid [44] and cis-plasmid with either ChRmine or ChReef under the control of human synapsin or CAG promotor. Cells were regularly tested for mycoplasma contamination. Viral particles were harvested cells and medium; precipitated from medium with 40% polyethylene glycol 8000 (Acros Organics, Germany) in 500mM NaCl and combined with cell pellets for processing. Pellets were suspended in 500mM NaCl, 40mM Tris, 2.5mM MgCl2, pH 8, and 100 Uml−1 of salt-activated nuclease (Arcticzymes, USA) at 37 °C for 30 min. Cleared lysates were purified over iodixanol (Optiprep, Axis Shield, Norway) step gradients (15%, 25%, 40%, and 60%) at 350,000 × g for 2.25 h. rAAV containing fractions were concentrated using Amicon filters (EMD, UFC910024) and formulated in sterile phosphate-buffered saline (PBS) supplemented with 0.001% Pluronic F-68 (Gibco, Germany). Viral vector titers were determined by the number of DNase I resistant vg using AAV titration kit (TaKaRa/Clontech) by qPCR (StepOne, Applied Biosystems) according the manufacturer’s instructions or with adaptations to usage in crystal digital PCR (dPCR) system. Here, dilutions of purified vector DNA were subjected to crystal dPCR using 5x Naica PCR reaction mix (Stilla, R10056) supplemented with primers provided in the AAV titration kit, 0,8mg/µl Alexa 647 (Invitrogen, 11570266) and 1.5x Eva Green (Biotum, #31000-T). Formation of droplet crystals and PCR was performed in a Naica Geode (Stilla) using Naica Ruby or Sapphire Chips (Stilla) and finally analyzed in the Naica Prism3 reader (Stilla) equipped with Crystal Reader and Crystal Miner softwares (Stilla). rAAVs titers and quantification method used is indicated for each rAAV in the respective methods chapter. Purity of produced viral vectors was routinely checked by silver staining (Pierce, Germany) after gel electrophoresis (Novex™ 4–12% Tris–Glycine, Thermo Fisher Scientific) according to the manufacturer’s instruction. Viral vector stocks were kept at −80 °C until injection. In summary, final constructs used for gene therapy in rodents consisted of ChRmine (mice) or ChReef (mice and gerbils) under control of the human synapsin (neuronal targeting) or CAG promoter (cardiac cluster stimulation) tagged with enhanced yellow fluorescent protein (eYFP) with enhancement of trafficking signal (TS) and ER export signal (ES) packed into PHP.eB for vision restoration experiments, for stimulation of the auditory pathway: AAV2/9 for mice and or PHP.S for gerbils, an in AAV2/9 for cardiac cell cluster stimulation.

Animals

All animal experiments were carried out in compliance with the relevant national and international guidelines (European Guideline for animal experiments 2010/63/EU) as well as in accordance with German laws governing animal use. The procedures have been approved by the responsible regional government office Rodents were kept in a 12h light/dark cycle with ad libitum access to food and water.

Preparing neonatal mouse cardiomyocytes

Hearts were explanted from p0-p3 mice killed by decapitation and directly placed on ice cold PBS. Remaining tissue and atria were carefully removed, and ventricular cardiomyocytes isolated with the neonatal heart dissociation kit for mouse and rat (Miltenyi, Germany). 1.5 – 2 million cells were plated on a 6-well-plate coated with 10 µg/ml fibronectin (Sigma; F1141-5MG) and maintained in IMDM (GlutaMAX, no phenol red; Gibco 21056-023) supplemented with 10% FBS superior (Sigma; S0615) and 1% Penicillin/Streptomycin (Life Technologies; 15140122) in standard cultivation conditions (37°C, 5% CO_2). One day later, medium was exchanged to reduce FBS to 0.5% and AAV transduction was performed with AAV2/9-CAG-ChRmine-TS-EYFP-ES with

$1.1x10^{10}$ GC/ml (qPCR) and AAV2/9-CAG-ChReef-TS-EYFP-ES with $6x10^{10}$ GC/ml (qPCR) corresponding to ~226 and ~69vp/cell, respectively. On day 3, the cells were dissociated and plated on Ø 10 mm round coverslips in cardiac cell clusters compromising 50.000 cells within 15 µl locally on a 8 µl 0.1% gelatine drop. Cells were incubated in this small drop for 20 min to build cardiac clusters and afterwards medium filled up in the well. After 1-2 days cardiac cell cluster started to beat spontaneously and 0.5% FBS IMDM medium was exchanged every 2-3 days.

Analysis of optogenetically evoked contraction of cardiac cell clusters

Experiments with beating cardiac cell clusters were performed between day 3 and 5 after plating with continuous perfusion with Tyrode solution (comprising 140 mM NaCl, 5.4 mM KCl, 1.8 mM $CaCl_2$, 2 mM $MgCl_2$, 10 mM glucose, and 10 mM HEPES; pH 7.4, adjusted with NaOH) to keep the cells at approximately 35 ° C. Electrical stimulation (0.2 ms long biphasic pulses, 45 V) was performed with two platinum electrodes and the Myostim stimulator (Myotronic, Germany) and light stimulation with a LedHub (Omicron). 510 nm light was generated by a 500 – 600 nm LED, filtered through a ET500/20 excitation filter and reflected onto the cells via a 561 nm beamsplitter (AHF, F38-561). 625 nm light was generated with the 625 LED through a 635/18 excitation filter and reflected onto the cells via a 409/493/573/652 beamsplitter (AHF, F68-409) within an inverted IX73 microscope and through a 20x objective (LUCPLFLN20XPH/0,45). Imaging light was filtered by a 780 nm long pass filter (Schott RG780) to avoid excitation of ChRmine and ChReef by the illumination and images were taken with a UI-306xCP-M camera (iDS, Germany) and analysed online with the custom made Myocyte online Contraction Analysis (MoCA) software recently described in detail[45] giving the absolute average of motion vectors per frame |V| as output through NI 9263 CompactDAQ (NI, Austin, U.S.) recorded with Powerlab 8/35 and LabChart 8.1.16 software for analysis. The software and Powerlab were also used to trigger electrical pacing and LEDs . Light intensity was calibrated with the S170C sensor and Powermeter (Thorlabs, Germany).

To determine the threshold of optical pacing, cardiac cell clusters were illuminated by ten consecutive light pulses (5 ms for 510 nm; 50 ms for 625 nm) with the indicated repetition rates. Light intensity was lowered stepwise to the light intensity at which pacing capability was lost. The lowest intensity capable to trigger contractions 1:1 with the last 8 of 10 light pulses was defined as pacing threshold. The defibrillation capability was tested during supramaximal electrical pacing (45 V, 0.2 ms biphasic) at a repetition rate 0.5 Hz above the spontaneous beating frequency. 5 s long light pulses were used, and defibrillation defined as successful, when electrical stimulation failed to induce any detectable contraction during the illumination period.

Histology for cardiomyocytes

Neonatal heart cells were fixed in 4% formaldehyde for 20 min, permeabilised with 0.2% Triton X100 for 20 min and stained in DPBS (Sigma; D8537) supplemented with 5% donkey serum for 2 h with primary antibodies against cardiac troponin I (ab47003, Abcam: 1:800) and for 1 h with secondary antibodies conjugated with Cy5 (711-175-152, JacksonLab, U.S., 1:400) diluted in DPBS with 1:1000 DAPI (0018860.01, Th.Geyer) at room temperature. Images of single cardiomyocytes for analysis of expression rate were taken through a 10x (10X/NA 0,4 Olympus UPLSAPO) or 20x objective (20x/NA 0,7 Olympus UCPLFLN PH) with an IX83 inverted fluorescence microscope equipped with an ORCA-flash 4.0 digital camera (C11440, Hamamatsu Photonics) and the MT20 illumination system as light source controlled via the CellSens® software. Acquisition of images was performed with following filter settings: 387/11 excitation, 410 beamsplitter and 440/40 emission for DAPI, 485/20, 504 and 525/30 for eYFP, 560/25, 582, and 684/24 for Cy5. Transduction rate was calculated by the percentage of eYFP positive cells among all cardiomyocytes identified by cardiac troponin I antibody-staining.

Cardiomyocyte clusters were imaged with a LSM 800 confocal microscope (Zeiss) equipped with spectral multi-alkali photomultiplier detectors. Z-stack acquisition was performed using a Plan-Apochromat 20x/0.8 M27 via the ZEN 2.6 (blue edition) software (Zeiss) with a pinhole of 55 µm for Dapi, 24 µm for eYFP, 27 µm for the red channel and 31 µm to image Cy5. Pictures were post-processed using stack correction (Background+Decay+Flickr), extended depth of focus (Wavelets, highest Z-Stack Alignment) and Image calculator (subtraction of autofluorescence) of the Zen 3.4 (blue edition) software.

Statistics of optogenetic stimulation of cardiac tissue

All dots represent the individual result from one cardiac cell cluster and the mean is shown with the standard error of the mean as bars. Statistical analysis was performed with a 2-way ANOVA with Holm-Sidak multiple comparison test for the optical pacing, unpaired students t-test for the defibrillation with 510 nm as well as the expression rate, and Fisher´s exact contingency test for the defibrillation capability with 625 nm.

Methods for optogenetic stimulation of visual system

Intravitreal injection

3-months old female and male Rd1 (C3HeB/FeJ, JAX 000658) mice were anesthetized with a subcutaneous injection of a fentanyl (0.05 mg/kg), midazolam (5 mg/kg), and medetomidine (0.5 mg/kg) (FMM) cocktail. Mice were then secured using a bite bar and placed on top of a temperature controller (Supertech) to maintain a body temperature of 37°C. For local anesthesia of the eyes, eye drops containing 0.5% Proxymetacain were applied and hydration gel (Bayer, Bepanthen) was placed on the eyes to prevent dryness whenever possible. Before injection, a hole posterior to the ora serrata was created using a 27-gauge needle. Then, a Hamilton syringe was guided through this hole into the intravitreal space and 2µl of virus solution of PHP.eB-hsyn-ChRmine-TS-EYFP-ES (1,89E+13 GC/ml, dPCR) or PHP.eB-hsyn-ChReef-TS-EYFP-ES (8,59E+13 GC/ml, dPCR) was injected at 4µl/min using a motorized injector (Stoelting). After 5 min the syringe was withdrawn and the anesthesia was reversed with a subcutaneous injection of a naloxone (1.2 mg/kg), flumazenil (0.5 mg/kg), and atipamezole (2.5 mg/kg) cocktail.

Optical stimulation

For visual stimulation at different light intensities, a LED (530nm, Thorlabs, M530L4) in combination with a filter wheel and 6 different neutral density filters (Thorlabs, FW1AND) was used. Light intensities were measured using a digital optical power and energy meter (Thorlabs, PM100D). Green light was presented to the contralateral eye from a distance of 2cm while the eye ipsilateral to the recording site was covered. Visual stimulation was timed (200ms at 1Hz) using a pre-programmed pulse generator (Doric, OTPG_8), which was synchronized with the electrophysiological recordings. Accordingly, for visual stimulation using a screen, white full field flashes (200ms at 1Hz) were presented using PsychoPy[46] on an IPad screen (LG LP097QX1) 5cm from the contralateral eye. A photodiode was used to synchronize the visual stimulation with the electrophysiological recordings.

Electrophysiological recordings

To enable stable fixation in the recording setup, a head-post was implanted onto the skull of vision restored mice at least 5 days before electrophysiological recordings using standard surgical procedures. To record neural activity, 32-channel silicon probes (Cambridge NeuroTech, type H10b) with a 32-channel headstage (Intan technologies, C3324) were connected via a SPI interface cable (Intan technologies, C3216) to an USB interface board (Intan technologies, C3100). Data was recorded at 20 kHz using RHX software. Mice were anesthetized using FMM cocktail and head-fixed in a holding tube. The head of the mouse was aligned in all three axes to the coordinate system of the probe manipulator. Openings in the skull above the primary visual cortex (AP: 3.9 mm, ML: 2.1mm) were created using a drill, and the probe was lowered into V1 at a speed of 2 μm/s. Data was acquired at different depths (DV: -0.4 mm to -0.8 mm below the brain surface) in both hemispheres during separate recordings and stimulation of the contralateral eye. Electrophysiological recordings were performed 10 min after reaching the desired depth. CM-Dil (Thermo Fisher, CellTracker) was applied to the probe prior to brain insertion to allow post-hoc confirmation of the recording site.

Analysis of optogenetic stimulation of visual system

Electrophysiological recordings were analyzed using kilosort3[47], and spike sorting results were manually curated using the phy software (https://github.com/cortex-lab/phy). Only units with stable responses across the duration of the session and high kilosort quality scores were included in subsequent analysis. To obtain continuous firing rate estimates, single unit responses were binned with a bin size of 1 ms and convolved with a gaussian kernel with a standard deviation of 10 ms. Trial-averaged responses were normalized to the mean and standard deviation of the baseline (400ms before stimulus onset) across all intensities. Units that did not respond to the highest light intensity were excluded (mean normalized firing rate during the stimulus smaller than 2.58). The Gramm toolbox[48] was used to visualize raster plots. For significance testing across time points a permutation based method[49] was used as described[50]. Briefly, using unpaired t-tests differences between the two conditions for each time point are determined and subsequently time clusters are identified using the bwconncomp.m function in Matlab (4 connected components). Time cluster significance is determined by comparison the t-statistics of the actual data against the t-statistics of shuffled data (10000 permutations with randomized labels).

Histology and imaging after optogenetic stimulation of visual system

To visualize retinal expression patterns, eyes of vision restored animals after the electrophysiological experiments were collected and fixed in 4% PFA for 1h at RT. After washing in PBS, retinas were prepared and fixed again for 10 min in 4% PFA at RT. Fixed and washed retinas were put in 30% Sucrose and subjected two three rounds of freezing and thawing on dry ice. Then retinas were incubated for 1h in 10% normal donkey serum (NDS) and subsequently in primary antibody solution (rabbit-GFP (Proteintech, 50430-2-AP), 1:666 in PBS with 3% NDS and 0.5% Triton-X) for 4 days at 4°C. After incubation, retinas were washed in PBS and incubated in secondary antibody overnight at 4°C (AlexaFluor 488 (Invitrogen, A32970), 1:500 in PBS with 3% NDS and 0.5% Triton-X). Finally, washed retinas were mounted in DAPI-containing Vectashield (Vector Laboratories, H-1200).

For post-hoc analysis of recording sites, brains were collected and incubated in 4% PFA at 4°C overnight. Then brains were washed and embedded in 4% agarose. 100µm coronal slices were cut using a vibratome (Leica microsystems, VT1000S) and stained for 2h at RT (DAPI, Thermo Fisher Scientific, D1306, 2.5 µg/ml). Washed brain slices were mounted on microscope slides in Vectashield (Vector Laboratories, H-1200).

Tiled images were captured using a Leica TCS SP8 laser scanning confocal microscope with a 20× oil immersion (NA 0.75) or a 10× air (NA 0.3) objective (Leica Microsystems). Images were merged and processed using LAS X (Leica Microsystems) and Adobe Photoshop software.

Optogenetic stimulation of auditory pathway

Postnatal AAV injection into the cochlea

The same injection approach was performed for all animals which later would be subject to either: auditory brainstem recordings, juxtacellular recordings from single putative SGNs, *ex vivo* acute slice electrophysiology in mice, or recordings from the inferior colliculus in Mongolian gerbils. AAV injections into the left ear were performed at postnatal day 6 in C57BL/6 wild-type mice or at postnatal day 6.33±0.46 days in Mongolian Gerbils[18,43]. The right ear served as a non-injected control. In brief, mouse and gerbil pups were randomly selected for virus injections. Under general isoflurane anesthesia (5% for anesthesia induction, 1–3% for maintenance with frequent monitoring of the hind-limb withdrawal reflex and anesthesia adjustments, accordingly) and local xylocaine as well as buprenorphine (0.1 mg/kg) and carprofen (5 mg/kg) for analgesia, the cochlea of the left ear was accessed via a retroauricular incision. Body temperature was maintained at physiological temperature. The cochlea was gently punctured using a borosilicate capillary pipette, which was kept in place to inject the virus of following titers:

Mice: AAV2/9-hsyn-ChRmine-TS-EYFP-ES 5.1x10^{13} GC/ml (qPCR), AAV2/9-hsyn-ChReef-TS-EYFP-ES 3.1x10^{13} (qPCR) and 2.45x10^{13} GC/ml (dPCR)

Gerbil: PHP.S-hsyn-ChReef-TS-EYFP-ES 5.25 x10^{13}GC/ml (qPCR)

After virus injection the tissue in the injection area was repositioned and the wound was sutured. Carprofen (5 mg/kg) was administered for analgesia the day after surgery.

Optical stimulation of the auditory pathway *in vivo*

The left cochlea was exposed by performing a retroauricular incision behind the pinna followed by a bullostomy, where the round window was visualized and punctured. For mice a 50 µm optical fiber coupled to a 594 nm (OBIS LS OPSL, 100 mW, Coherent Inc., Santa Clara, United States) or a 522 nm (Oxxius combined with a motorized Power Attenuator, Lannion, France) diode laser was used. For gerbils a 200 µm optical fiber was only coupled to the prior mentioned 522 nm laser. Laser power was calibrated prior to each experiment using a laser power meter (Thorlabs PM100USB).

Optically evoked auditory brainstem responses in mice

Data were obtained from 40 adult C57Bl/6 wild-type mice of either sex (22 male, 18 female). 78.9 ± 26.3 days after virus injection (see: postnatal AAV injection into the cochlea) mice were subjected to *in vivo* optical stimulation and recordings. Surgeries and measurements were performed under anesthesia using isoflurane (5% for anesthesia induction, 1–3% for maintenance with frequent monitoring of the hind-limb withdrawal reflex and anesthesia adjustments, accordingly) and analgesia by sub-cutaneous injections of buprenorphine (0.1 mg/kg body weight) and meloxicam (5 mg/kg body weight). Body temperature was maintained at 37°C using a custom-designed heat plate through all the procedures.

Stimulus generation and delivery, as well as data acquisition was performed using a custom-written software (MATLAB, MathWorks, Natick, MA, United States) employing National Instrument data acquisition cards and a custom-build laser-controller. Recordings were conducted in a soundproof chamber (IAC Acoustics, IL, United States). Optically evoked ABRs (oABRs) and acoustically evoked ABRs (aABRs) were recorded by placing needle electrodes behind the pinna, on the vertex, and on the back of the anesthetized mice. The difference in potential between the vertex and mastoid subdermal needles was amplified using a custom-designed amplifier, sampled at a rate of 50 kHz for 20 ms, filtered (300–3000 Hz) and averaged across 1000 stimulus presentations. The ABRs threshold was defined and determined as the lowest light or sound intensity for which one of the 3 waves was reliably visible. The latency of a given wave was defined as the time delay between the stimulus onset and the peak of the wave of interest. The amplitude was defined as the difference response strength between positive peak (P) and the negative (N), of a wave of interest.

Data analysis of optically evoked auditory brainstem responses in mice

The mouse ABR data was analyzed using custom-made Matlab software (The MathWorks, Inc., Natick, MA, USA). Averages were expressed as mean ± standard deviation. For statistical comparison between two groups, data sets were tested for equality of variances (F-test) followed by two-tailed unpaired Student’s t-test.

Juxtacellular recordings from optically driven single putative SGNs in mice

Data were obtained from 2 adult mice 86 and 88 days after AAV injection (see: postnatal AAV injection into the cochlea). Mice were anesthetized with an intraperitoneal injection of xylazine (5 mg/kg) and urethane (1.32 g/kg), and analgesia was achieved with sub-cutaneous administration of buprenorphine (0.1 mg/kg, maintenance dose administered every 4h) and carprofen (5mg/kg). Body temperature was maintained at 37°C using a custom-designed heat plate through all the procedures.

The experimental/ surgical procedure consisted of the following steps: 1) The left cochlea was exposed via a bulleostomy and the round window membrane was made visible. For one mouse the cochlea was acutely deafened, following application of kanamycin (200 mg/ml). 2) The optical fiber was placed in the round window niche (see methods, Optical stimulation *in vivo*). 3) After positioning the fiber or 10 minutes after kanamycin application, optically induced oABRs were recorded and their threshold was determined. 4) The optical fiber was taken out, and the animal underwent a tracheotomy procedure and was subsequently intubated. 5) The animal was positioned in a custom-designed stereotactic head holder. 6) The optical fiber was placed in the round window niche (see methods, Optical stimulation *in vivo*). 7) Following removal of the pinnae, the scalp was reflected and portions of the lateral interparietal and left occipital bone were removed. Next, the cerebellum was partially aspirated to expose the left semi-circular canal. A reference electrode was placed on the contralateral muscles behind the right ear and was constantly maintained in a moist state to ensure optimal contact. Utilizing the left semi-circular canal as a reference point, a micromanipulator (Luigs Neumann SM 10) was employed to insert a borosilicate glass capillary into the cochlear meatus (WPI 1B120F-4, length 100mm, OD 1.5mm, ID 0.84mm). 8) The optical stimulus consisted of laser pulses with a duration of 1ms, a stimulation rate of 20Hz, and radiant flux of 6mW. Using the micromanipulator's step function, putative optically sensitive spiral ganglion neurons (SGNs) were identified. Action potentials were amplified using an ELC-03XS amplifier (NPI Electronic, Tamm, Germany), filtered (300–20000 Hz), digitized (National Instruments card PCIe-6323), analysed, and prepared for display using custom-written MATLAB (The MathWorks, Inc.) software.

Data analysis of juxtacellular recordings from optically driven single putative SGNs in mice

In accordance with prior work[38], neurons were classified as putative SGNs if they met the following criteria: i) they exhibited a monophasic and ii) positive waveform, iii) were recorded at a depth exceeding 1000µm below the cerebellum surface, and iv) displayed a first spike latency of less than 3ms in response to a 1ms light pulse presented at 6mW.

We detected the initial spike that followed each stimulus and calculated both its average latency and latency jitter, represented by the standard deviation of the first spike latency. Additionally, we computed the vector strength and spikes per pulse by examining the discharge rate starting 150 ms into the stimulus train and extending it for the entire 350 ms stimulation train. This analysis characterizes the neuronal discharge during the adapted state of the neuron.

For estimating the light intensity threshold, the laser intensity was gradually lowered until there were no more time-locked responses during the adapted state of the neuron. This protocol was only completed for six recorded neurons.

Ex vivo acute slice electrophysiology

At the age of 20 – 23 days, two weeks after AAV injection (see: postnatal AAV injection into the cochlea), brainstem slices were prepared as previously described[51]. In brief, the brain was immediately immersed in ice cold cutting solution (Supplementary Table 4) and pinned, dorsal side down, on a wax stage. With the ventral side of the brainstem exposed, the meninges were removed with curved forceps and a mid-sagittal cut was performed using a straight razor, splitting the brain in two hemispheres. Scissors were used to cut between the cerebellum and the occipital lobe of each hemisphere in order to separate the hind-brain from the fore-brain. The two blocks of hind-brain, containing brain-stem and cerebellum, were glued with cyanoacrylate glue, (Loctite 401, Henkel) medial side down, on the stage of a Leica (Wetzlar, Germany) VT 1200 vibratome. The lateral side of both brain blocks was facing upwards and was facing towards the advancing blade. A vibration amplitude of 1.5mm was used and the blade was placed at the height of the cerebellar flocculus. Cerebellar tissue was sectioned at an advancing speed of 0.05 – 0.1 mm/s and discarded. Thereafter, a speed of 0.02mm/s was used to obtain 150µm thick parasagittal slices of the cochlear nucleus. The slices were incubated in artificial cerebro-spinal fluid (aCSF, Table S4) for a total of 30 minutes in a 35°C water bath (Julabo, Seelbach, Germany), after which they were maintained in aCSF at room temperature (23 – 25 °C) until recording. The pH of both the cutting solution and the aCSF was adjusted to 7.4. The osmolarity was, in mOsm, 310 for the aCSF and 320 for the cutting solution. Both solutions were continuously aerated with carbogen (95% O_2, 5% CO_2). An EPSC10 USB patch clamp amplifier was used for all recordings and was driven by the Patchmaster Next software (HEKA Elektronik GmbH, Reutlingen, Germany). The sampling interval was set to 25µs and the filter at 7.3 kHz. For better visualization of the slice's cell layers and auditory nerve fibers (ANFs), differential interference contrast (DIC) microscopy was used on upright Olympus BX51WI microscope with a water immersion LUMPLFLN40XW objective (Olympus, Hamburg, Germany). All recordings were performed at near physiological temperature (33 – 35°C). The bath solution flowed through an inline solution heater (SC-20 with CL-200A controller; Warner Instruments, Hamden, CT, USA). The temperature of the solution was monitored by a thermistor placed between the opening of the inflow tube and the slice in the recording chamber.

Borosilicate filamentous glass capillaries (GB150F, Inner diameter: 0.86mm | Outer Diameter: 1.50mm | Length: 80mm, Science Products GmbH, Hofheim, Germany) were used to pull patch pipettes on a P-1000 micropipette puller (Sutter Instruments Co., Novato, CA, USA). The resistance at the tip of the pipette was strictly 2 – 3 MΩ to avoid increases of the series resistance (R_s) over long recordings. The pipettes were filled with intracellular solution (details on Table S4), which additionally contained 1mM of Alexa – 568 (Invitrogen / Fisher Scientific, Schwerte, Germany). The pH of the solution was adjusted to 7.4 and its osmolarity to 325 mOsm, to prevent osmotic collapse of the patched neuron, preserve the cell's vigour and prevent fluctuations of the R_s over long recordings. Voltage clamp experiments were performed with a V_{hold} = -70mV, corrected for a liquid junction potential of 12mV. Only cells with R_s values less than 8 MΩ were included in the analysis. Afferent fiber optogenetic stimulation was performed using a green laser included in the Oxxius multi-wavelength bundle (LBX-488-40-CSB, maximum Power: 40mW; LCX-532-50CSB, maximum power: 50mW; OBIS-594-100, maximum power: 100mW; LBX-638-100-CSB, maximum power: 100mW; Laser 2000 GmbH, Wessling, Germany). Synapses were driven with trains of stimuli yielding varying success rates, hereafter termed oEPSC probability. oEPSC probability (P_{oEPSC}) was defined as $\frac{Number\ of\ oEPSCS}{50}$, 50 signifying the number if 1ms light pulses that were delivered to the ANF. Minimal stimulation irradiance was defined as the lowest value that could yield a P_{oEPSC} = 1 at 10 Hz. This irradiance value was used later in the experiment to assess the P_{oEPSC} at higher frequencies. For ANF stimulation, 5, 10, 20, 33, 40, 50 and 100 Hz were the tested frequencies. In direct transduction experiments, where the photocurrent properties of ChReef were measured, 10, 20, 30, 50, 100, 200, 300 and 350 Hz were used instead. Electrophysiology data were analysed using Igor Pro (Wavemetrics, Lake Oswego, OR, USA). Evoked release was analysed using custom Igor scripts. Confocal z-stacks were processed with the NIH ImageJ software[52]. Figures were assembled for display using open-source vector graphic software Inkscape (https://inkscape.org).

Immunohistochemistry and immunofluorescence imaging for acute slice electrophysiology

The 150 µm thick slices that were used for electrophysiological recordings were fixed for 30 minutes in Formaldehyde (FA) at room temperature after the experiment. Afterwards they were washed in PBS for 10 minutes to halt fixation and blocked with GSDB for 1 hour at room temperature. After fixation the slides were kept for 10 minutes in ice cold PBS to halt fixation and then washed for 1 hour at room temperature in goat serum dilution buffer, which contained in 16% normal goat serum, 450 mM NaCl, 0.3% Triton X-100, and 20 mM phosphate buffer (PB, pH 7.4). The slides were then incubated in primary antibodies diluted in GSDB, for 3 hours, in a wet chamber at room temperature. Four washing steps followed, that lasted 10 minutes each, two of them with Wash Buffer (450 mM NaCl, 0.3% Triton X-100 and 20mM PB) and two more with PBS. The slides were then incubated with secondary antibodies overnight at 4°C and, afterwards, washed twice with Wash Buffer and twice more with PBS as before. Before mounting, the slides were maintained in 5mM PB for 10 minutes and were then mounted with a drop of Mowiol (Carl

Roth GmbH, Karlsruhe, Germany) and covered with a thin glass coverslip. Double sided tape spacers of 120µm thickness were used for mounting to flank the slice before the application of Mowiol. This way, the coverslip's weight would not be applied fully on the slice, avoiding extra vertical pressure, which resulted in better preservation of structural integrity of the tissue.

Immunofluorescence imaging was performed on a Zeiss LSM 780 Microscope with a 40x NA1.4 *Oil* Plan-Apochromat objective. *Primary antibodies:* chicken-anti-GFP (1:500, Abcam, Berlin, Germany), guinea-pig-anti-vGLUT1 (1:1000, Synaptic Systems GmbH, Göttingen, Germany). *Secondary antibodies:* goat-anti-chicken 488 (1:200, Thermo Fisher Scientific, Waltham, USA) goat-anti-guinea-pig 568 (1:200, Thermo Fisher Scientific, Waltham, USA).

Inferior colliculus recordings during optical stimulation of the cochlea in the Mongolian gerbil

Multi-channel recordings of neuronal clusters were performed in the tonotopically organized central nucleus of the inferior colliculus (IC) of Mongolian gerbils at the age of 71 ± 11 days; while stimulating SGNs optically or acoustically as previously described[32]. Briefly, a craniotomy was performed on the right hemisphere of the animal's skull to access the IC, contralateral to the injected ear. A linear 32-electrode silicon probe (Neuronexus, Ann Arbor, USA) was positioned above the brain ~2mm lateral to lambda and the probe was slowly inserted ~3.3mm into the brain (measured from the surface of visual cortex) using a micromanipulator. Mapping of recording sites was done using acoustic stimuli (Fig. S13) and the probe was further advanced (or retracted) accordingly. Recordings were performed using a Digital Lynx 4S recording system

(Neuralynx; Dublin, Ireland) along with custom-built hardware, in combination with custom-written and established MATLAB software.

Data analysis of inferior colliculus recordings

The recorded signal from the 32 channels was bandpass filtered between 600 and 6000 Hz, digitized and spike times were computed as any waveform crossing three times the mean absolute deviation of the signal (MAD). A one millisecond refractory period was included to not overestimate the spike count of the signal. Post-stimulus time histograms (PSTH) were computed by binning spike counts in 0.2 millisecond bins. The first three consecutive bins crossing threshold of 3x MAD indicate t_{on} and, respectively, the last three consecutive bins over threshold indicate t_{off}. Based on the time window extracted, the signal was further analyzed and sorted in a two-dimensional matrix according to stimulus intensity and corresponding recording site. From this matrix, we calculated the cumulative distribution index (d') based on spike rates calculated across increasing intensities starting with 0 intensity condition. This indicates a change/increase in the neuronal firing rate in relation to baseline levels i.e. a d' of 1 indicates an increase in firing rate of 1 standard deviation from baseline and distinguish triggered signals from noise[32]. Based on these computed matrixes, iso-contour lines at integer d' values were constructed and minimums specify thresholds to d' indicated.

To analyze temporal properties, responsive recording channels were extracted and channels reaching a d' of 1 when optically stimulating at 1 mW were analyzed further. To calculate the number of spikes per stimulus, we divided the spike counts recorded by the number of repeats per recording and by the number of pulses from stimulation rate used To calculate the vector strength, a measure of spike timing relative to stimulation cycle the following formula was previously[37]:

$$VS = \frac{\sqrt{[\sum_{i=1}^{n} \cos \theta i]^2 + [\sum_{i=1}^{n} \sin \theta i]^2}}{n} \qquad \text{[Equation 7]}$$

With θ describing the spike timing computed from stimulus onset to following stimulus onset for a given stimulus cycle (phase). The Rayleigh test (eq. 8) was then performed in order to test the significance of vector strength for each unit and each repeat.

$$L = 2 * length(\theta i) * (VS^2) \qquad \text{[Equation 8]}$$

If $L<13.8$, $p>0.001$ and vector strength significance is rejected and set to 0. Firing rates were computed across all recordings by dividing the spike counts recorded in the determined spike window by the duration of that spike window. These values were normalized to the highest firing rate recorded for plotting.

Immunostaining and confocal imaging of cochlear cryosections from mice and Mongolian gerbils

Directly after the end of the optogenetic measurements, cochleae from both sides were prepared as previously described[14,18,36]. In short, samples were fixed for an hour in 4% paraformaldehyde (PFA), decalcified for 3-4 days in 0.12 M ethylenediaminetetraacetic acid (EDTA), dehydrated in 25% sucrose solution for 24 hours and cryosectioned (mid-modiolar cryosections, 25 µm tick). Immunofluorescence staining were done in 16% goat serum dilution buffer (16% normal goat serum, 450 mM NaCl, 0.6% Triton X-100, 20 mM phosphate buffer, pH 7.4). The following primary antibodies were used at 4 °C overnight: chicken anti-GFP (1:500, ab13970 Abcam, USA) and guinea pig anti-parvalbumin (1:300, 195004 Synaptic Systems, Germany); and secondary antibodies for one hour in room temperature: goat anti-chicken 488 IgG (1:200, A-11039 Thermo Fisher Scientific, USA) and goat anti-guinea pig 568 IgG (1:200, A-1107 Thermo Fisher Scientific, USA). Finally, slices were mounted in Mowiol 4-88 (Carl Roth, Germany). Samples were imaged with a confocal microscope SP8 (Leica, Germany) mounted with a 40x oil objective. For each cochlear turn (apex, middle and base) an image was taken focusing on the modiolus.

Analysis of immunostaining and confocal imaging of cochlear cryosections

Image analysis was performed by a custom-written MATLAB script modified from[43]. Briefly, SGN somas and modiolus area were manually detected using a touch screen from the parvalbumin images. Next, individual somas were automatically segmented using Otsu's threshold method from every Z-stack and a mask corresponding to the given SGN was defined for the Z-stack for which the mask was fulfilling the criteria of size (area and diameter) and circularity. In case the segmentation was not correct, the segmentation of the given SGN soma was performed manually. Next, the median GFP brightness of each SGNs was measured and its distribution was fitted with a Gaussian mixture model with up to 3 components. A threshold, above which SGNs somas were considered as transduced, was defined as average + 3 x standard deviation of the Gaussian distribution with the lowest mean.

Data availability statement: The data that support the findings of this study is available from the corresponding authors upon reasonable request.

Code availability statement: The code used for analysis is available from the corresponding authors upon reasonable request.

Acknowledgements

We thank Christiane Senger-Freitag for expert help with cloning of the ChR constructs and excellent technical support. The authors gratefully acknowledge Daniela Gerke for virus production and histology of auditory samples. We further gratefully acknowledge Anupriya Thirumalai for assistance image analysis. We thank Gerhard Hoch for excellent technical support, and Patricia Räke-Kügler for excellent administrative support. We thank Julia Kuhl for her help on figure illustrations. The European Research Council through the Advanced Grant ‘OptoHear” to TM under the European Union's Horizon 2020 Research and Innovation program (grant agreement No. 670759) as well as in the project OptoWave (ERC Proof-of-Concept grant, Horizon 2022). Further support came from German Research Foundation through the Cluster of Excellence (EXC2067) Multiscale Bioimaging (TM, TMa, TB, EM) and the Leibniz Program to TM. Furthermore this work was also supported by the Ernst Jung Prize for Medicine and by Fondation Pour l'Audition (FPA RD-2020-10) and received funding by Volkswagen-Stiftung from the "Niedersächsisches Vorab" (ZN3898 and ZN4000) (to TM). AG was supported by Alexander von Humboldt Foundation. VH and FE are fellows of the German Academic Scholarship Foundation (Studienstiftung des Deutschen Volkes). TB was supported and funded by the German Centre for Cardiovascular Research (DZHK), the Deutsche Forschungsgesellschaft (DFG, German Research

Foundation: Germany's Excellence Strategy (EXC 2067/1-390729940), IRTG1826 (200857327, Svenja Kiehn); Priority Program 1926 (315212873), CRC1002 (193793266, project A14), clinician scientist program 413501650 to MH and project 452139556. D.S. was supported by the Swiss National Science Foundation (SNSF) Early Postdoc Mobility no. 194957, SNSF Postdoc. Mobility no. 211087 and Deutsche Forschungsgemeinschaft Walter-Benjamin Programm (Stelle) no. SI 2831/1-1.

Author contributions

TM, TMa, BW, EM and TB designed the research. ChR construct design and mutagenesis were conducted by TMa. In vitro characterization was a collaborative effort by MZ, AA, AG and IW under supervision of TMa. Virus design and production was done by KK. Optogenetic cardiac stimulation experiments were performed by MH, SMK, and TB. Optogenetic vision restoration research was undertaken by DS, ST, and EM. VH, TA, FE, AV, and BW performed the optogenetic stimulation of the auditory periphery with supervision of TM. MZ, TH, AA, AV, FE, DS, TB and TA prepared figures with input from other authors. TM und TMa wrote the paper with contributions of EM, TB and BW. TM, EM and TB acquired funding. All authors have reviewed and approved the final version of the manuscript for submission.

Competing interests

TM is co-founder of the OptoGenTech Company. TM, MZ and TMa are authors on a pending patent application related to this work, filed by Universitaetsmedizin Goettingen and OptoGenTech (EPA-22155173). Remaining authors declare no conflict of interest.

References

1. Emiliani, V. *et al.* Optogenetics for light control of biological systems. *Nat. Rev. Methods Primer* **2**, 1–25 (2022).

2. Sahel, J.-A. *et al.* Partial recovery of visual function in a blind patient after optogenetic therapy. *Nat. Med.* **27**, 1223–1229 (2021).
3. Feldbauer, K. *et al.* Channelrhodopsin-2 is a leaky proton pump. *Proc. Natl. Acad. Sci.* **106**, 12317–12322 (2009).
4. Kleinlogel, S., Vogl, C., Jeschke, M., Neef, J. & Moser, T. Emerging Approaches for Restoration of Hearing and Vision. *Physiol. Rev.* **100**, 1467–1525 (2020).
5. Dieter, A., Keppeler, D. & Moser, T. Towards the optical cochlear implant: optogenetic approaches for hearing restoration. *EMBO Mol. Med.* **12**, e11618 (2020).
6. Govorunova, E. G., Sineshchekov, O. A., Janz, R., Liu, X. & Spudich, J. L. Natural light-gated anion channels: A family of microbial rhodopsins for advanced optogenetics. *Science* **349**, 647–650 (2015).
7. Govorunova, E. G. *et al.* Kalium channelrhodopsins are natural light-gated potassium channels that mediate optogenetic inhibition. *Nat. Neurosci.* **25**, 967–974 (2022).
8. Marshel, J. H. *et al.* Cortical layer–specific critical dynamics triggering perception. *Science* **365**, eaaw5202 (2019).
9. Kishi, K. E. *et al.* Structural basis for channel conduction in the pump-like channelrhodopsin ChRmine. *Cell* **185**, 672-689.e23 (2022).
10. Sineshchekov, O. A. *et al.* Conductance Mechanisms of Rapidly Desensitizing Cation Channelrhodopsins from Cryptophyte Algae. *mBio* **11**, 10.1128/mbio.00657-20 (2020).
11. Hsueh, B. *et al.* Cardiogenic control of affective behavioural state. *Nature* **615**, 292–299 (2023).
12. Chen, R. *et al.* Deep brain optogenetics without intracranial surgery. *Nat. Biotechnol.* **39**, 161–164 (2021).
13. Gradinaru, V. *et al.* Molecular and Cellular Approaches for Diversifying and Extending Optogenetics. *Cell* **141**, 154–165 (2010).

14. Keppeler, D. *et al.* Ultrafast optogenetic stimulation of the auditory pathway by targeting-optimized Chronos. *EMBO J.* **37**, e99649 (2018).
15. Yoshino, M. & Murakami, K. Analysis of the substrate inhibition of complete and partial types. *SpringerPlus* **4**, 292 (2015).
16. *Single-channel recording*. (Springer, 2009).
17. Kleinlogel, S. *et al.* Ultra light-sensitive and fast neuronal activation with the Ca^2+-permeable channelrhodopsin CatCh. *Nat. Neurosci.* **14**, 513–518 (2011).
18. Mager, T. *et al.* High frequency neural spiking and auditory signaling by ultrafast red-shifted optogenetics. *Nat. Commun.* **9**, 1750 (2018).
19. Saita, M. *et al.* Photoexcitation of the P4480 State Induces a Secondary Photocycle That Potentially Desensitizes Channelrhodopsin-2. *J. Am. Chem. Soc.* **140**, 9899–9903 (2018).
20. Kuhne, J. *et al.* Unifying photocycle model for light adaptation and temporal evolution of cation conductance in channelrhodopsin-2. *Proc. Natl. Acad. Sci.* **116**, 9380–9389 (2019).
21. Bruegmann, T. *et al.* Optogenetic defibrillation terminates ventricular arrhythmia in mouse hearts and human simulations. *J. Clin. Invest.* **126**, 3894–3904 (2016).
22. Nyns, E. C. A. *et al.* Optogenetic termination of ventricular arrhythmias in the whole heart: towards biological cardiac rhythm management. *Eur. Heart J.* **38**, 2132–2136 (2017).
23. Crocini, C. *et al.* Optogenetics design of mechanistically-based stimulation patterns for cardiac defibrillation. *Sci. Rep.* **6**, 35628 (2016).
24. Bruegmann, T., Beiert, T., Vogt, C. C., Schrickel, J. W. & Sasse, P. Optogenetic termination of atrial fibrillation in mice. *Cardiovasc. Res.* **114**, 713–723 (2018).
25. Nyns, E. C. A. *et al.* An automated hybrid bioelectronic system for autogenous restoration of sinus rhythm in atrial fibrillation. *Sci. Transl. Med.* **11**, (2019).

26. Richter, C. & Bruegmann, T. No light without the dark: Perspectives and hindrances for translation of cardiac optogenetics. *Prog. Biophys. Mol. Biol.* **154**, 39–50 (2020).
27. Sasse, P., Funken, M., Beiert, T. & Bruegmann, T. Optogenetic Termination of Cardiac Arrhythmia: Mechanistic Enlightenment and Therapeutic Application? *Front. Physiol.* **10**, 675 (2019).
28. Pyari, G., Bansal, H. & Roy, S. Ultra-low power deep sustained optogenetic excitation of human ventricular cardiomyocytes with red-shifted opsins: a computational study. *J. Physiol.* **600**, 4653–4676 (2022).
29. Chang, B. *et al.* Retinal degeneration mutants in the mouse. *Vis. Res* **42**, 517–525 (2002).
30. Norton, T. T. & Siegwart, J. T. Light levels, refractive development, and myopia--a speculative review. *Exp. Eye Res.* **114**, 48–57 (2013).
31. Wolf, B. J. *et al.* Is there an unmet medical need for improved hearing restoration? *EMBO Mol. Med.* **14**, e15798 (2022).
32. Dieter, A., Duque-Afonso, C. J., Rankovic, V., Jeschke, M. & Moser, T. Near physiological spectral selectivity of cochlear optogenetics. *Nat. Commun.* **10**, 1962 (2019).
33. Dieter, A. *et al.* µLED-based optical cochlear implants for spectrally selective activation of the auditory nerve. *EMBO Mol. Med.* e12387 (2020) doi:10.15252/emmm.202012387.
34. Saeedi, A., Englert, L. & Hemmert, W. eABR THR Estimation Using High-Rate Multi-Pulse Stimulation in Cochlear Implant Users. *Front. Neurosci.* **15**, 705189 (2021).
35. Taberner, A. M. & Liberman, M. C. Response Properties of Single Auditory Nerve Fibers in the Mouse. *J. Neurophysiol.* **93**, 557–569 (2005).
36. Bali, B. *et al.* Utility of red-light ultrafast optogenetic stimulation of the auditory pathway. *EMBO Mol. Med.* **13**, e13391 (2021).
37. Wrobel, C. *et al.* Optogenetic stimulation of cochlear neurons activates the auditory pathway and restores auditory-driven behavior in deaf adult gerbils. *Sci. Transl. Med.* **10**, eaao0540 (2018).

38. Mittring, A., Moser, T. & Huet, A. T. Graded optogenetic activation of the auditory pathway for hearing restoration. *Brain Stimulat.* **16**, 466–483 (2023).
39. Friesen, L. M., Shannon, R. V. & Cruz, R. J. Effects of stimulation rate on speech recognition with cochlear implants. *Audiol. Neurootol.* **10**, 169–184 (2005).
40. Marshel, J. H. *et al.* Cortical layer–specific critical dynamics triggering perception. *Science* **365**, eaaw5202 (2019).
41. Klapoetke, N. C. *et al.* Independent optical excitation of distinct neural populations. *Nat. Methods* **11**, 338–346 (2014).
42. Nagel, G. *et al.* Channelrhodopsin-2, a directly light-gated cation-selective membrane channel. *Proc. Natl. Acad. Sci. U. S. A.* **100**, 13940–13945 (2003).
43. Huet, A. T. & Rankovic, V. Application of Targeting-Optimized Chronos for Stimulation of the Auditory Pathway. in *Methods in Molecular Biology (Clifton, N.J.)* vol. 2191 261–285 (2021).
44. Challis, R. C. *et al.* Systemic AAV vectors for widespread and targeted gene delivery in rodents. *Nat. Protoc.* **14**, 379–414 (2019).
45. Wagdi, A. *et al.* Selective optogenetic control of Gq signaling using human Neuropsin. *Nat. Commun.* **13**, 1765 (2022).
46. Peirce, J. *et al.* PsychoPy2: Experiments in behavior made easy. *Behav. Res. Methods* **51**, 195–203 (2019).
47. Pachitariu, M., Sridhar, S. & Stringer, C. Solving the spike sorting problem with Kilosort. 2023.01.07.523036 Preprint at https://doi.org/10.1101/2023.01.07.523036 (2023).
48. Morel, P. Gramm: grammar of graphics plotting in Matlab. *J. Open Source Softw.* **3**, 568 (2018).
49. Maris, E. & Oostenveld, R. Nonparametric statistical testing of EEG- and MEG-data. *J. Neurosci. Methods* **164**, 177–190 (2007).

50. Cazemier, J. L. *et al. Involvement of superior colliculus in complex figure detection of mice*. http://biorxiv.org/lookup/doi/10.1101/2022.09.25.509365 (2022) doi:10.1101/2022.09.25.509365.

51. Butola, T. *et al.* RIM-Binding Protein 2 Organizes Ca2+ Channel Topography and Regulates Release Probability and Vesicle Replenishment at a Fast Central Synapse. *J. Neurosci.* **41**, 7742–7767 (2021).

52. Schneider, C. A., Rasband, W. S. & Eliceiri, K. W. NIH Image to ImageJ: 25 years of image analysis. *Nat. Methods* **9**, 671–675 (2012).

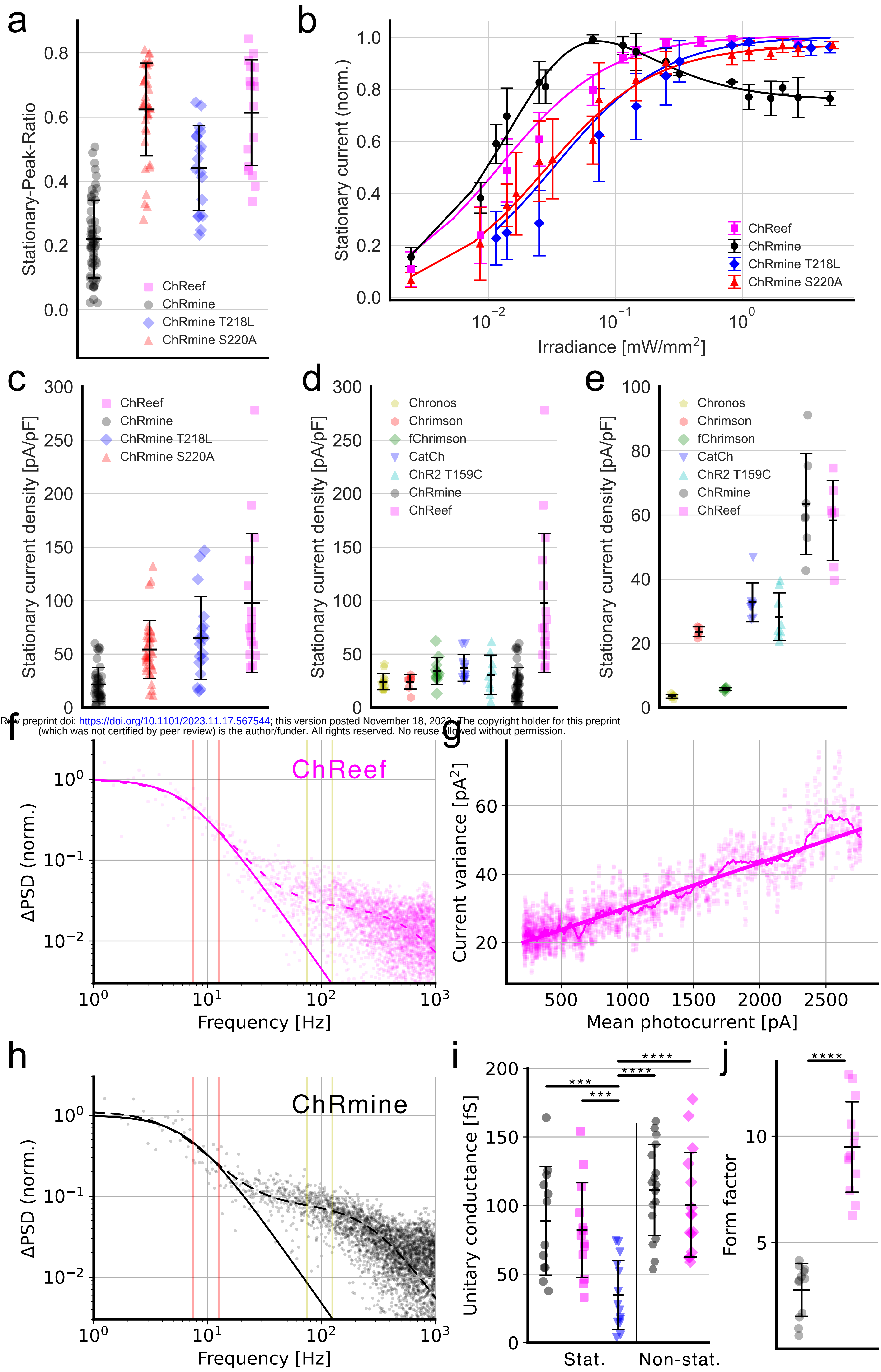
a
Stationary-Peak-Ratio
0.0
0.2
0.4
0.6
0.8
ChReef
ChRmine
ChRmine T218L
ChRmine S220A
b
Stationary current (norm.)
0.0
0.2
0.4
0.6
0.8
1.0
10^{-2}
10^{-1}
10^{0}
Irradiance [mW/mm^2]
ChReef
ChRmine
ChRmine T218L
ChRmine S220A
c
Stationary current density [pA/pF]
0
50
100
150
200
250
300
ChReef
ChRmine
ChRmine T218L
ChRmine S220A
d
Stationary current density [pA/pF]
0
50
100
150
200
250
300
Chronos
Chrimson
fChrimson
CatCh
ChR2 T159C
ChRmine
ChReef
e
Stationary current density [pA/pF]
0
20
40
60
80
100
Chronos
Chrimson
fChrimson
CatCh
ChR2 T159C
ChRmine
ChReef
f
ChReef
ΔPSD (norm.)
10^{0}
10^{-1}
10^{-2}
10^{0}
10^{1}
10^{2}
10^{3}
Frequency [Hz]
g
Current variance [pA^2]
20
40
60
500
1000
1500
2000
2500
Mean photocurrent [pA]
h
ChRmine
ΔPSD (norm.)
10^{0}
10^{-1}
10^{-2}
10^{0}
10^{1}
10^{2}
10^{3}
Frequency [Hz]
i
Unitary conductance [fS]
0
50
100
150
200
***
***
****
****
Stat.
Non-stat.
j
Form factor
5
10
****

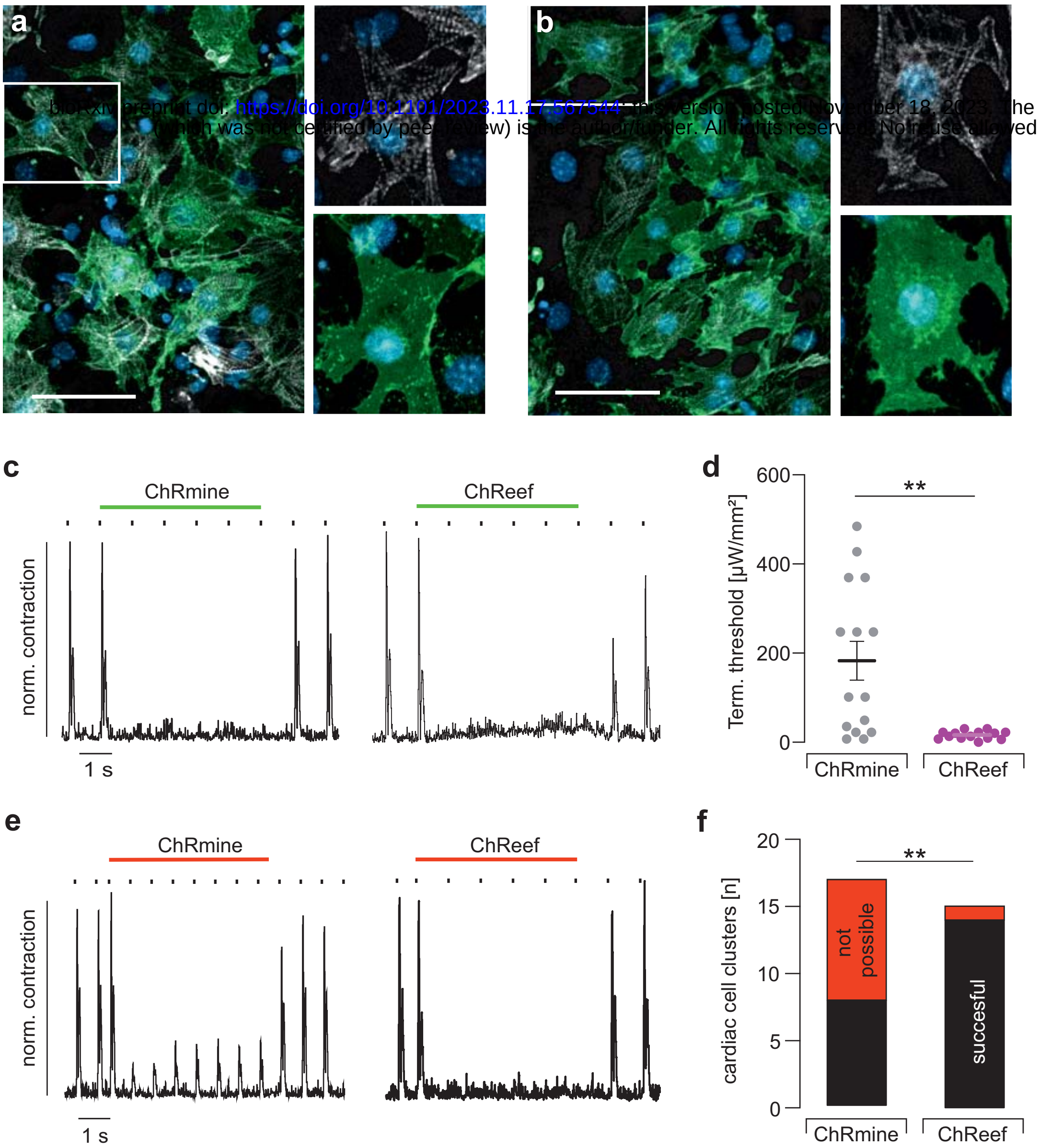
a
b
c
ChRmine
ChReef
norm. contraction
1 s
d
600
400
200
0
Term. threshold [µW/mm²]
**
ChRmine
ChReef
e
ChRmine
ChReef
norm. contraction
1 s
f
20
15
10
5
0
cardiac cell clusters [n]
**
not possible
succesful
ChRmine
ChReef

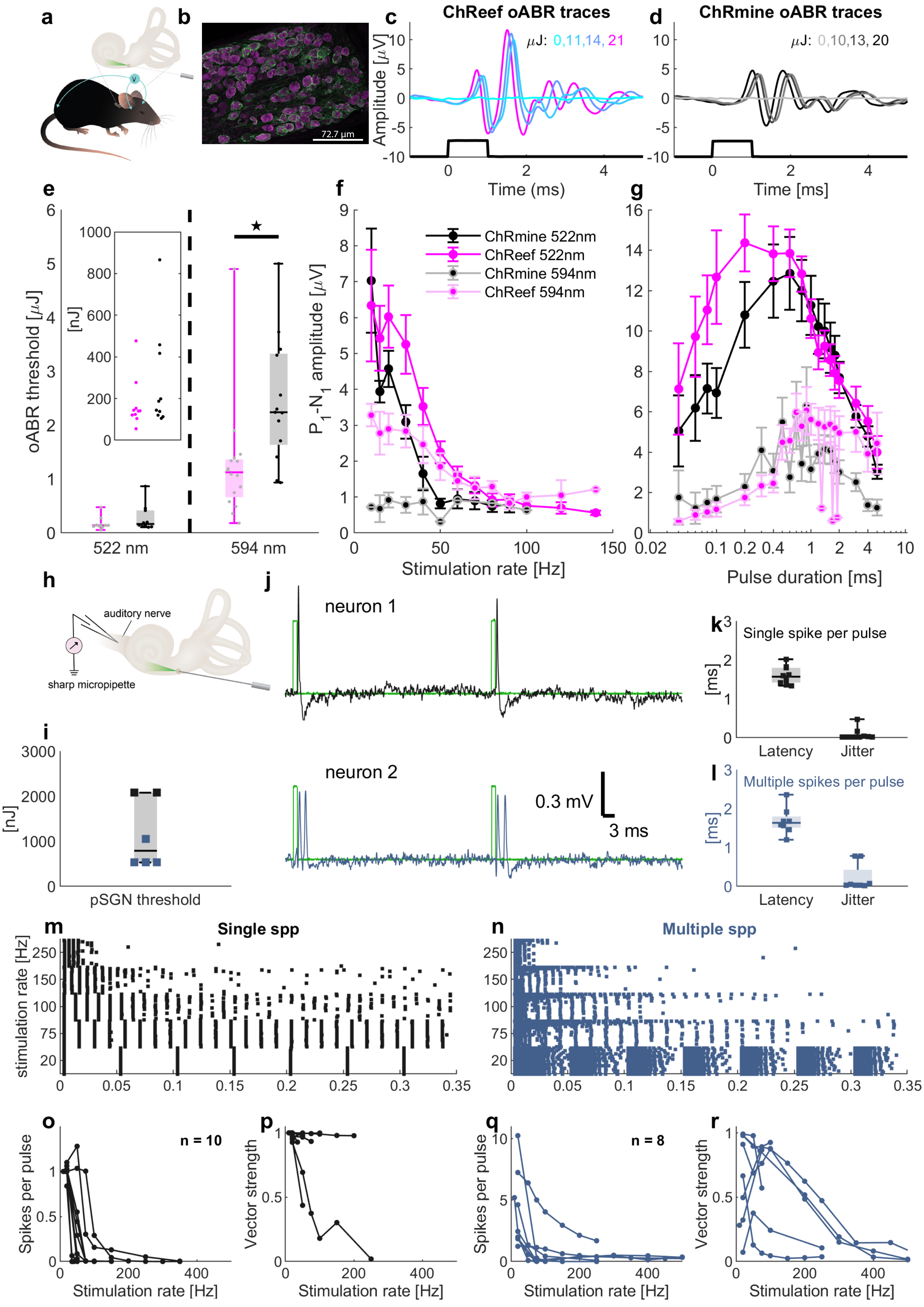
a
b
72.7 µm
c
ChReef oABR traces
µJ: 0,11,14, 21
Amplitude [µV]
Time (ms)
d
ChRmine oABR traces
µJ: 0,10,13, 20
Time [ms]
e
oABR threshold [µJ]
[nJ]
522 nm
594 nm
f
ChRmine 522nm
ChReef 522nm
ChRmine 594nm
ChReef 594nm
P1-N1 amplitude [µV]
Stimulation rate [Hz]
g
Pulse duration [ms]
h
auditory nerve
sharp micropipette
i
[nJ]
pSGN threshold
j
neuron 1
neuron 2
0.3 mV
3 ms
k
Single spike per pulse
[ms]
Latency
Jitter
l
Multiple spikes per pulse
[ms]
Latency
Jitter
m
Single spp
stimulation rate [Hz]
n
Multiple spp
o
n = 10
Spikes per pulse
Stimulation rate [Hz]
p
Vector strength
Stimulation rate [Hz]
q
n = 8
Spikes per pulse
Stimulation rate [Hz]
r
Vector strength
Stimulation rate [Hz]

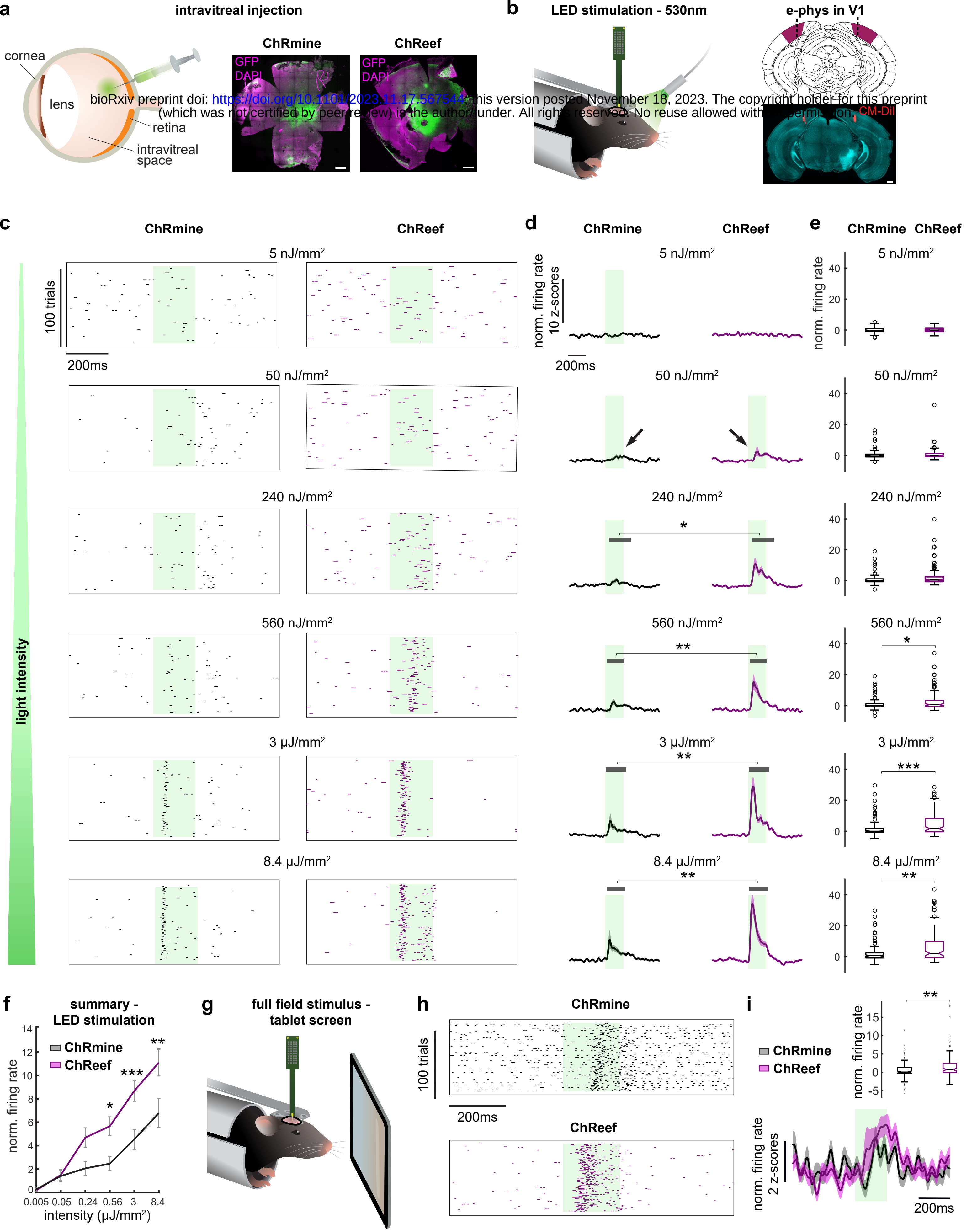
a
intravitreal injection
cornea
lens
retina
intravitreal space
ChRmine
ChReef
GFP
DAPI
b
LED stimulation - 530nm
e-phys in V1
CM-DiI
c
ChRmine
ChReef
light intensity
100 trials
200ms
5 nJ/mm²
50 nJ/mm²
240 nJ/mm²
560 nJ/mm²
3 µJ/mm²
8.4 µJ/mm²
d
ChRmine
ChReef
norm. firing rate
10 z-scores
200ms
*
**
e
ChRmine ChReef
norm. firing rate
40
20
0
*
***
**
f
summary - LED stimulation
ChRmine
ChReef
norm. firing rate
intensity (µJ/mm²)
0.005 0.05 0.24 0.56 3 8.4
0 2 4 6 8 10 12 14
*
***
**
g
full field stimulus - tablet screen
h
ChRmine
ChReef
100 trials
200ms
i
ChRmine
ChReef
norm. firing rate
15 10 5 0 -5
**
norm. firing rate
2 z-scores
200ms

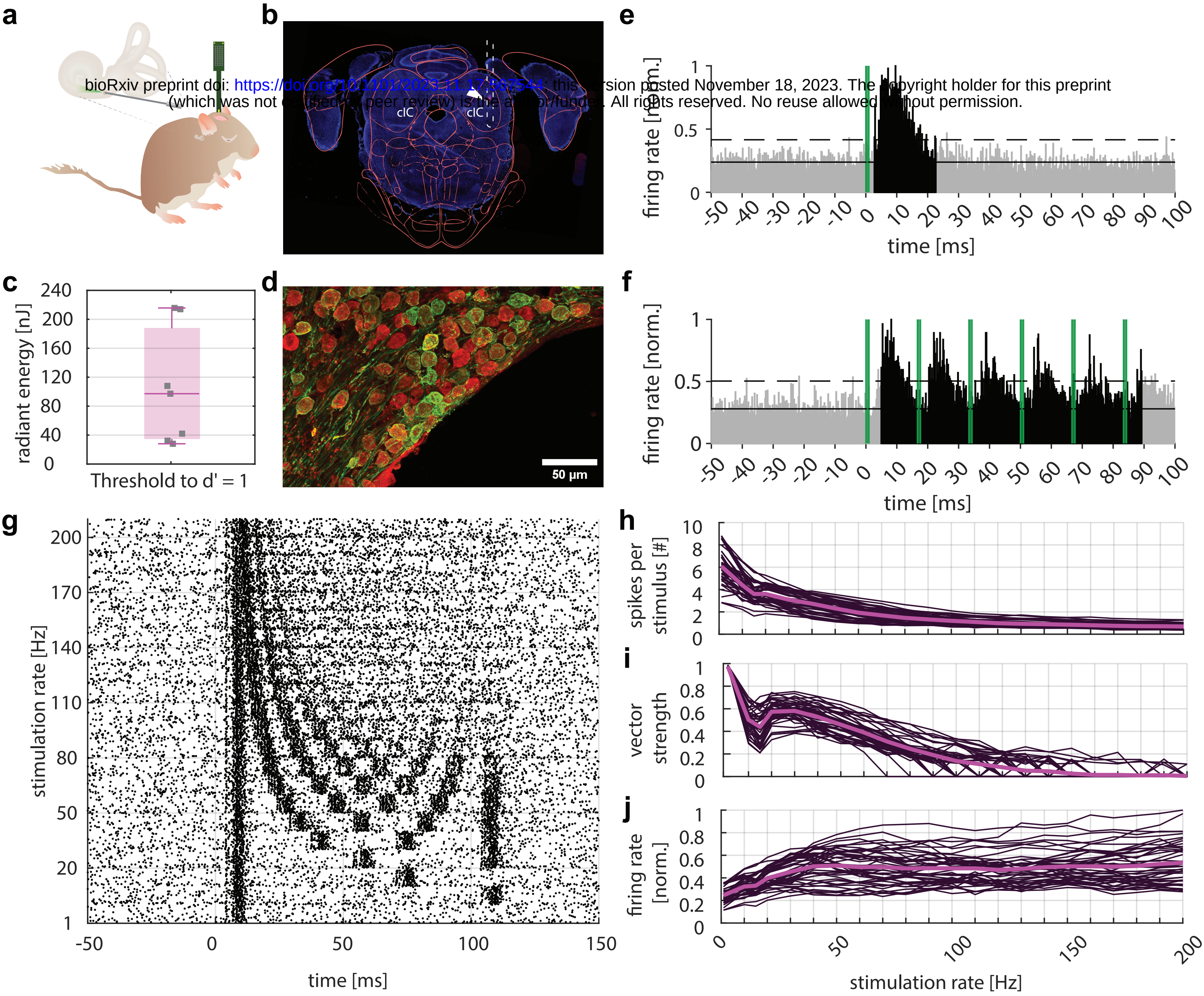
a
b
cIC
cIC
e
firing rate [norm.]
1
0.5
0
-50 -40 -30 -20 -10 0 10 20 30 40 50 60 70 80 90 100
time [ms]
c
radiant energy [nJ]
240
200
160
120
80
40
0
Threshold to d' = 1
d
50 µm
f
firing rate [norm.]
1
0.5
0
-50 -40 -30 -20 -10 0 10 20 30 40 50 60 70 80 90 100
time [ms]
g
stimulation rate [Hz]
200
170
140
110
80
50
20
1
-50 0 50 100 150
time [ms]
h
spikes per stimulus [#]
10
8
6
4
2
0
i
vector strength
1
0.8
0.6
0.4
0.2
0
j
firing rate [norm.]
1
0.8
0.6
0.4
0.2
0
0 50 100 150 200
stimulation rate [Hz]